DOI: https://doi.org/10.2138/am-2020-7351. http://www.minsocam.org/

Revision 1-shortened version

Magma oxygen fugacity of mafic-ultramafic intrusions in convergent margin settings: insights for the role of magma oxidation states on magmatic Ni-Cu sulfide mineralization

Yonghua Cao [1, 2], Christina Yan Wang [1, 2]*, Bo Wei [1, 2]

[1] CAS Key Laboratory of Mineralogy and Metallogeny, Guangzhou Institute of Geochemistry, Chinese Academy of Sciences, Guangzhou 510640, China

[2] Guangdong Provincial Key Laboratory of Mineral Physics and Materials, Guangzhou 510640, China

Corresponding author: Dr. C.Y. Wang (wang_yan@gig.ac.cn)

Abstract

Oxygen fugacities (fO_2) of mantle-derived mafic magmas have important controls on the sulfur status and solubility of the magmas, which are key factors to the formation of magmatic Ni-Cu sulfide deposits, particularly those in convergent margin settings. In order to investigate the fO_2 of mafic magmas related to Ni-Cu sulfide deposits in convergent margin settings, we obtained the magma fO_2 of a number of Ni-Cu sulfide-bearing mafic-ultramafic intrusions in the central Asian orogenic belt (CAOB), North China, based on the olivine-spinel oxygen barometer and the modeling of V partitioning between olivine and melt. We also calculated the mantle fO_2 on the basis of V/Sc ratios of primary magmas of these intrusions.

Ni-Cu sulfide-bearing mafic-ultramafic intrusions in the CAOB include arc-related Silurian-Carboniferous ones and post-collisional Permian-Triassic ones. Arc-related intrusions formed before the closure of the paleo-Asian ocean and include the Jinbulake, Heishan, Kuwei and Erbutu intrusions. Post-collisional intrusions were emplaced in extensional settings after the closure of the paleo-Asian ocean and include the Kalatongke, Baixintan, Huangshandong, Huangshan, Poyi, Poshi, Tulaergen and Hongqiling No.7 intrusions. It is clear that the magma fO_2 values of all these intrusions in both settings range mostly from FMQ+0.5 to FMQ+3 and are generally elevated with the fractionation of magmas, much higher than that of MORBs (FMQ-1 to FMQ+0.5). However, the mantle fO_2 values of these intrusions vary from ~FMQ to ~FMQ+1.0, just slightly higher than that of MORBs (≤ FMQ). This slight difference is interpreted as the intrusions in the CAOB may have been derived from the metasomatized mantle wedges where only minor slab-derived, oxidized components were involved. Therefore, the high magma fO_2 values

of most Ni-Cu sulfide-bearing mafic-ultramafic intrusions in the CAOB were attributed to the fractionation of magmas derived from the slightly oxidized metasomatized mantle. In addition, the intrusions that host economic Ni-Cu sulfide deposits in the CAOB usually have magma fO_2 of >FMQ+1.0 and sulfides with mantle-like $\delta^{34}S$ values (-1.0 to +1.1‰), indicating that the oxidized mafic magmas may be able to dissolve enough mantle-derived sulfur to form economic Ni-Cu sulfide deposits. Oxidized mafic magmas derived from metasomatized mantle sources may be an important feature of major orogenic belts.

Keywords: Mafic-ultramafic intrusion; Magmatic Ni-Cu sulfide mineralization; Magma oxygen fugacity; Central Asian orogenic belt; Convergent margin setting

INTRODUCTION

The oxygen fugacity (fO_2) of mantle-derived mafic magmas is controlled by equilibria of Fe^{3+}-Fe^{2+} and S^{2-}-S^{6+} (Kress and Carmichael, 1991; Jugo et al., 2005), and can be quantified as $\triangle\log fO_2$ relative to mineral assemblage buffers. The fO_2 values of mafic magmas are considered to be closely related to geodynamic settings, but how they differ in different settings is still a matter of debate. In general, having $Fe^{3+}/\sum Fe$ and $S^{6+}/\sum S$ higher than the mid-ocean ridge basalts (MORBs), arc and back-arc basalts may have formed from relatively oxidized magmas (Wood et al., 1990; Nilsson and Peach, 1993; Jugo et al., 2010; Brounce et al., 2017). It has been demonstrated that arc and back-arc basalts were derived from metasomatized mantle wedges that have been oxidized to variable degrees (Debret et al., 2016; Rielli et al., 2017; Bénard et al., 2018). It is also known that the metasomatized mantle beneath subduction zones has fO_2 similar to the mantle beneath the mid-ocean ridges, and it is the fractionation of metasomatized mantle-derived magmas or the interaction of hydrated magmas with ambient mantle that elevated the magma fO_2 (Lee et al., 2005, 2010; Dauphas et al., 2010; Tollan and Hermann, 2019; Li et al., 2020).

Magmatic Ni-Cu sulfide deposits are traditionally thought to be related to the mafic magmatism induced by either mantle plumes or rifting within intraplate settings (Naldrett, 2004). However, mafic-ultramafic intrusions in convergent margin settings have become targets for prospecting economic Ni-Cu sulfide deposits in recent years (Maier et al., 2008; Thakurta et al., 2008; Tomkins et al., 2012; Manor et al., 2016; Song et al., 2016). The mantle sources of such intrusions in are generally considered to be metasomatized by slab-derived fluids/melts (Manor et al., 2016; Song et al., 2016). The mafic magmas derived from the metasomatized mantle can be highly hydrated and oxidized with fO_2 being up to FMQ+6 (FMQ means fayalite-magnetite-quartz oxygen buffer) (Kelley and Cottrell, 2009; Kelley et al., 2010; Gaillard et al., 2015). For example, the magma fO_2 of the Alaskan-type Duke intrusion in USA and the Turnagain and Mascot Ni-Cu sulfide-bearing mafic-ultramafic intrusions in Spain are calculated to be >FMQ+2 (Thakurta et al., 2008; Manor et al., 2016). The central Asian orogenic belt (CAOB) is one of the largest accretionary orogens in the world, resulted from large-scaled subduction and accretion of juvenile materials from Neoproterozoic to Paleozoic (Sengör et al., 1993; Xiao et al., 2004a, b, 2009; Jahn et al., 2004). A preliminary study on the oxidation states of a few Ni-Cu sulfide-bearing mafic-ultramafic intrusions in the CAOB indicates that magma fO_2 values vary from FMQ+0.3 to FMQ+2.6, much higher than that of MORBs (Cao et al., 2019).

Experimental results indicate that the sulfur solubility of highly oxidized mafic magmas can be as high as 1.4 wt.% with sulfur being dominantly as sulfate species (S^{6+}) (Jugo et al., 2005; Jugo, 2009), significantly higher than that of reduced mafic magmas with dominantly S^{2-} phases (Jugo et al., 2010; Cottrell and Kelley, 2011). Therefore, the oxidized mantle source or highly oxidized, hydrated mafic magmas may be more favorable for the magmatic Ni-Cu sulfide deposits in convergent margin settings (Jenner et al., 2010; Tomkins et al., 2012; Cao et al., 2019; Wei et al., 2019). However, the linkage between magma fO_2 of mafic-ultramafic intrusions and Ni-Cu sulfide mineralization is not well understood. Three important issues that should be answered: (1) if the mantle sources of the mafic-ultramafic intrusions in convergent margin settings have remarkably high fO_2 relative to those in intraplate settings? (2) if not, what triggers high magma fO_2 of the mafic-ultramafic intrusions in convergent margin settings? and (3) what is the favorable magma fO_2 for the Ni-Cu sulfide mineralization in convergent margin settings?

A number of Paleozoic mafic-ultramafic intrusions in the CAOB host Ni-Cu sulfide deposits with variable Ni grades and ore reserves, making up a ~4000-km-long Ni-Cu sulfide mineralization belt in North China. These intrusions were dated to be Devonian to Triassic in ages, some of which were emplaced in the subduction stage predating the closure of the paleo-Asian ocean, whereas others in the post-subduction, extensional stage after the closure of the paleo-Asian ocean (*e.g.,* Yang and Zhou, 2009; Qin et al., 2011; Li et al., 2012; Yang et al., 2012; Peng et al., 2013; Li et al., 2015). These intrusions are ideal to unravel the correlation between magma fO_2 and Ni-Cu sulfide mineralization in a convergent margin setting. In this study, we estimated the mantle and magma fO_2 of representative mafic-ultramafic intrusions in the CAOB that were emplaced in different ages and host variable degrees of Ni-Cu sulfide mineralization. The results indicate that most intrusions have magma fO_2 much higher than that of MORBs despite the similarity in their mantle fO_2. Such a feature can be further examined for the Ni-Cu sulfide-bearing mafic-ultramafic intrusions in convergent margin settings elsewhere.

GEOLOGICAL BACKGROUND

The central Asian orogenic belt is bounded by the Siberian Craton to the north and the Tarim Craton and North China Craton to the south (Fig. 1a). The belt extends for more than 7000 km from the Pacific ocean to the Eastern Europe, making up one of the largest accretionary orogenic belts on Earth. It formed due to the closure of the paleo-Asian ocean in Paleozoic and comprises numerous fragments of Precambrian microcontinents, Paleozoic island arcs, ophiolite suites, successions of volcanic rocks (Windley et al., 2007; Xiao et al., 2009).

The CAOB in China part is subdivided into the western and eastern segments (Zhou and Wilde, 2013) (Fig. 1b). The western segment is further divided into five belts, from north to south (Fig. 1c), including: 1) the Altay orogenic belt that is bounded by the Sayan belt to the north and by the Ulungar fault and Junggar block to the south (Sengör et al., 1993; Windley et al., 2002; Xiao et al., 2009), 2) the North Tianshan orogenic belt between the Junggar block to the north and the Aqikkuduk fault to the south (Zhou et al., 2004; Qin et al., 2011; Gao et al., 2012), 3) the Central Tianshan orogenic belt between the Aqikkuduk fault to the north and the Kawabulak fault to the south (Song et al., 2013),

4) the South Tianshan orogenic belt between the Kawabulak fault to the north and the Tarim Craton to the south (Yang and Zhou, 2009), and 5) the Beishan fold belt along the northeastern margin of the Tarim Craton (Xu et al., 2016). The eastern segment refers to the Xing'an-Mongolia orogenic belt in the Inner Mongolia and NE China (Zhang et al., 2015), which consists mainly of, from north to south, the Erguna massif, Xing'an massif, Songnen-Zhangguangcai range massif, and a continental margin accretionary belt (Wu et al., 2007) (Fig. 1d).

Numerous mafic-ultramafic intrusions that contain Ni-Cu sulfide mineralization occur in the CAOB. They were emplaced mainly in two periods, one from Silurian to Carboniferous and the other from Permian to Triassic (*e.g.,* Yang and Zhou, 2009; Xie et al., 2012; Hao et al., 2014; Mao et al., 2016).

Silurian to Carboniferous mafic-ultramafic intrusions

Silurian to Carboniferous mafic-ultramafic intrusions are mainly distributed in the western segment of the CAOB and host small- to medium-sized Ni-Cu sulfide deposits (Fig. 1b). As the paleo-Asian ocean was not yet closed until Permian in the western segment (Han et al., 2007; Xiao et al., 2009), these intrusions are considered to be arc-related (Yang and Zhou, 2009; Xie et al., 2012; Yang et al., 2012). Representative intrusions include the Jinbulake intrusion (ca. 430 Ma) in the central Tianshan belt (Yang and Zhou, 2009; Yang et al., 2012), the Kuwei intrusion (ca. 398 Ma) in the Altay belt (Li et al., 2015), and the Heishan intrusion (ca. 356 to 367 Ma) in the Beishan belt (Xie et al., 2012).

The parental magmas of these intrusions are tholeiitic (*e.g.,* Zhou et al., 2004; Yang and Zhou, 2009; Tang et al., 2012; Xia et al., 2013; Song et al., 2013). Rocks of these

DOI: https://doi.org/10.2138/am-2020-7351. http://www.minsocam.org/

intrusions have positive $\varepsilon_{Nd}(t)$ (+0.4 to +4) and initial Sr^{87}/Sr^{86} ranging from 0.704 to 0.709 (Yang and Zhou, 2009; Xie et al., 2012; Yang et al., 2012). They show depleted Nb and Ta relative to large ion lithophile elements (LILE) and light rare earth elements (LREE) on the primitive mantle-normalized trace element patterns (Fig. 2a-d), consistent with an arc-like affinity. These features were interpreted as magma generation from the depleted mantle that had been metasomatized by slab-derived fluids/melts (Yang and Zhou, 2009; Xie et al., 2012; Yang et al., 2012).

The Erbutu intrusion in the eastern segment of the CAOB is an outlier. Although it is dated to be 294.2±2.7 Ma, it is considered to be an arc-hosted intrusion (Peng et al., 2013). The intrusion hosts a small-sized Ni-Cu sulfide deposit and the parental magma is boninitic (Peng et al., 2013). The intrusion is mainly composed of olivine-bearing orthopyroxenite with mineral modes quite similar to those formed from boninitic magma (Peng et al., 2013). The rocks have LREE and LILE (*e.g.*, Ba and Rb) more enriched than those of the Jinbulake and Heishan intrusions (Fig. 2e, f).

Permian to Triassic mafic-ultramafic intrusions

Permian to Triassic mafic-ultramafic intrusions in the CAOB host a number of economic Ni-Cu sulfide deposits, including the Kalatongke intrusion (290-282 Ma) in the Altay belt (Song and Li, 2009; Zhang et al., 2009; Gao et al., 2012), the Huangshandong and Huangshanxi intrusions (274-283 Ma) in the Huangshan-Jingerquan mineralized belt in the North Tianshan belt (Qin et al., 2011; Sun et al., 2013), the Tulaergen intrusion (265±9.2 Ma) in the Kanggur-Huangshan shear zone in the North Tianshan belt (Zhao et al., 2017), the Poyi and Poshi intrusions (270-277 Ma) in the Beishan belt (Xue et al., 2016), and the Hongqiling No.7 and Piaohechuan No.4 intrusions (ca. 210-230 Ma) in the

Xing'an-Mongolia belt (Wei et al., 2013, 2015) (Fig. 1b). In addition, many other intrusions in this period host potential Ni-Cu sulfide mineralization, including the Huangshannan (278±2 Ma) and Baixintan intrusions (286±3 Ma) in the North Tianshan belt (Mao et al., 2016; Feng et al., 2017), the Luodong intrusion (260-290 Ma) in the Beishan belt (Su et al., 2015), and the Hongqiling No.1, 2, 3, 9, 32 and 33 intrusions (ca. 210-230 Ma) in the Xing'an-Mongolia belt (Hao et al., 2014).

These intrusions are considered to have formed in post-subduction, extensional settings after the closure of the paleo-Asian ocean (*e.g.,* Jiang et al., 2009; Li et al., 2012; Sun et al., 2013; Wei et al., 2013, 2015; Mao et al., 2014, 2015). The rocks of these intrusions show arc-like trace element patterns (Fig. 3a-d), which are attributed to the derivation from the metasomatized, depleted mantle (Xie et al., 2012; Li et al., 2012; Mao et al., 2014; Deng et al., 2015). However, the rocks of the Luodong intrusion have MORB-like, LREE-depleted trace element patterns (Fig. 3e, f), which may have been derived from the weakly metasomatized mantle (Su et al., 2015).

INTRUSIONS AND SAMPLES CHOSEN FOR OXYGEN FUGACITY CALCULATION

A prerequisite to use the olivine-spinel oxygen barometer is to obtain the compositions of equilibrated olivine-spinel pair in rocks (Ballhaus et al., 1991). The mafic-ultramafic intrusions in the CAOB that have rocks containing olivine-spinel pair include Silurian to Carboniferous Jinbulake, Heishan and Erbutu intrusions, and Permian to Triassic Baixintan, Huangshannan, Huangshandong, Huangshanxi, Poyi, Luodong, Tulaergen, Hongqiling No.1 and No. 2 intrusions. In this study, we calculated the magma

DOI: https://doi.org/10.2138/am-2020-7351. http://www.minsocam.org/

and mantle fO_2 values of the Jinbulake, Heishan, Erbutu, Baixintan, Huangshannan, Luodong, and Tulaergen intrusions. Together with the magma and/or mantle fO_2 values of the Huangshandong, Huangshanxi, Poyi and Hongqiling No.1 and No. 2 intrusions that were obtained in our earlier studies (Cao et al., 2019; Wei et al., 2019), an integrated framework of the magma and mantle fO_2 of the Ni-Cu sulfide-bearing mafic-ultramafic intrusions in the CAOB can be outlined. The results in this study are compared with the magma fO_2 values of the picrite in the Dali area, SW China, which is part of the Emeishan large igneous province (LIP) that formed within an intraplate setting. The petrography of the selected mafic-ultramafic intrusions in the CAOB and the Dali picrite in the Emeishan LIP were described in Supplementary Information.

ANALYTICAL RESULTS

Compositions of olivine-spinel pairs in mafic-ultramafic intrusions in the CAOB

The compositions of the olivine-spinel pairs in the rocks of the selected mafic-ultramafic intrusions in the CAOB were analyzed in this study. Analytical methods were described in Supplementary Information. The results of the olivine-spinel pairs are described in Supplementary Information and the data are listed in Table S1.

A summary of spinel compositions

The spinel grains from the mafic-ultramafic intrusions in either arc or post-subduction, extensional settings in the CAOB have highly variable Cr# and XFe^{3+}. The grains from the Erbutu intrusion have the highest Cr# and the lowest XFe^{3+} among the three arc-hosted intrusions (Fig. 4a, b). Among the intrusions in the post-subduction, extensional settings, the spinel grains from the Baixintan, Huangshannan and Tulaergen intrusions have relatively restricted Cr# but highly variable XFe^{3+} relative to those from the Luodong and Hongqiling No.1 and No.2 intrusions (Fig. 4a, b). In addition, the spinel grains from the Luodong intrusion has similar Cr# but relatively low and restricted XFe^{3+} compared to those from the Hongqiling No.1 and No.2 intrusions (Fig. 4a, b). The spinel grains from the Erbutu and Luodong intrusions are clustered on the plot of Mg# versus XFe^{3+}, whereas the grains from each of other intrusions generally show a negative trend of Mg# versus XFe^{3+}on this plot (Fig. 4b).

The spinel grains in the Dali picrite overall have higher Mg# and Cr#, and lower XFe^{3+} than those from the intrusions in the CAOB (Fig. 4a, b). However, they have similar Cr# and XFe^{3+} to those from the Erbutu intrusion (Fig. 4a, b). They display a nearly horizontal trend on the plot of Mg# versus XFe^{3+} (Fig. 4b), which is in contrast to the negative correlation trend for the spinel from the intrusions in the CAOB on the plot.

S isotope compositions of sulfides in mafic-ultramafic intrusions in the CAOB

The method of *in situ* S isotope analysis for the sulfides (pyrrhotite, pentlandite and chalcopyrite) in the rocks of the selected mafic-ultramafic intrusions in the CAOB is described in Supplementary Information. The sulfides in the wehrlite of the Jinbulake intrusion have $\delta^{34}S$ ranging from +0.3 to +1.3‰ (Table 1). The sulfides in the lherzolite of the Baixintan intrusion have $\delta^{34}S$ ranging from -0.7 to +1.2‰ (Table 1). The sulfides in the lherzolite of the Tulaergen intrusion have $\delta^{34}S$ ranging from -0.2 to +0.8‰ (Table 1). Overall, the sulfides from the three intrusions have a restricted range of $\delta^{34}S$ from -0.7 to +1.3‰. Likewise, the sulfides in the ores of three economic Ni-Cu sulfide deposits hosted in the Permian-Triassic Kalatongke, Hongqiling No. 7 and Piaohechuan No. 4 intrusions in the CAOB have $\delta^{34}S$ ranging from -1.0 to +1.1‰ (Wei et al., 2019). All of these values are similar to the $\delta^{34}S$ of MORB-type mantle (-1.5 to +0.6‰, Labidi et al., 2013, 2014) (Fig. 5). In contrast, the sulfides from the rocks of the Erbutu intrusion have $\delta^{34}S$ ranging from +5.3 to +7.5‰ (Table 1), much higher than those from other intrusions in the CAOB (Fig. 5).

CALCULATION RESULTS OF OXYGEN FUGACITY

The oxygen fugacity of the mantle and mantle-derived mafic magmas can be calculated in four different ways, including: 1) measuring $Fe^{3+}/(Fe^{3+}+Fe^{2+})$ of basalts or quenched basaltic glass (Kress and Carmichael, 1991; Kelley and Cottrell, 2009), 2) quantifying the partition coefficients of redox-sensitive elements (*e.g.*, V and Cr) in the differentiation of magma (Canil, 1997; Mallmann and O'Neill, 2009), 3) using oxygen barometers based on the chemical equilibria between mineral pairs (*e.g.*, olivine-spinel pair) (Ballhaus et al., 1991), and 4) calculating the ratios of redox sensitive/insensitive elements (*e.g.*, V/Sc, Fe^t/Zn) of primary magmas (Lee et al., 2005, 2010; Mallmann and O'Neill, 2009). The fourth method is exclusively used to estimate the mantle oxygen fugacity (Lee et al., 2005; Mallmann and O'Neill, 2009), however, the three others are applicable to calculate the fO_2 of both mantle and mantle-derived magmas, depending on that the examined objects are mantle xenoliths (*e.g.*, Ionov and Wood, 1992), or fractionated basalts/mafic-ultramafic intrusions (*e.g.,* Cao et al., 2019).

Mantle fO_2

Given that the mantle xenolith that can be directly used to calculate the mantle fO_2 are unavailable in the CAOB, we constrained the mantle fO_2 based on the relationship between the mantle fO_2 and the V/Sc ratios of primary magmas, an alternative method proposed by Lee et al. (2005) and Mallmann and O'Neill (2009). Because V is sensitive to redox and Sc is not, the V/Sc ratio of primary magma is mainly governed by fO_2 during partial melting of a given mantle lithology (Lee et al., 2005; Mallmann and O'Neill, 2009), and is not affected by temperature and pressure (Canil and Fedortchouk, 2000; Li, 2018). In addition, the V/Sc ratio of basaltic magma is not sensitive to the crystallization of olivine (Lee et al., 2005; Mallmann and O'Neill, 2009), the V/Sc ratio of the melt in equilibrium with the most primitive olivine in a mafic-ultramafic intrusion can be taken as the ratio of primary magma, particularly if olivine is the only cumulus phase. Therefore, we selected the samples from the Heishan, Huangshannan, Luodong, Poyi and Hongqiling No.2 intrusions in the CAOB that contain high Fo olivine (Fo = 86 to 90) as the only cumulus phase, the obtained V/Sc ratio of the melt in equilibrium with the olivine is analog to the V/Sc ratio of the primary magma of the intrusion.

As olivine is the only cumulus phase in the rocks, the concentrations of V and Sc of the melt can be calculated using the mass balance equation (Godel et al., 2011):

$$C_{\mathrm{WR}}^{V,Sc} = F_{\mathrm{Ol}} \times C_{\mathrm{Ol}}^{V,\,Sc} + (1\text{-}F_{\mathrm{Ol}}) \times C_{\mathrm{Liq}}^{V,\,Sc} \qquad (1)$$

where $C_{\mathrm{WR}}^{V,\,Sc}$ and $C_{\mathrm{Ol}}^{V,\,Sc}$ is the concentrations of V and Sc in the bulk rock and cumulus olivine, respectively. The fraction of olivine (F_{Ol}) can be estimated in two ways; one is to analyze the back-scattered electron (BSE) images or scan thin sections of the samples, the other is to use the mass balance of whole-rock MgO and FeO contents combined with the olivine-liquid exchange coefficient (*Kd*) (Li and Ripley, 2011). In this study, we integrated the two ways to obtain the F_{Ol} and then calculated the concentrations of V and Sc in the melt ($C_{\mathrm{Liq}}^{V,\,Sc}$) based on equation (1) (Table S2).

The V/Sc ratios of primary magmas would increase slightly with the degrees of partial melting of the mantle at a given mantle fO_2 when it is ≤FMQ, but would decrease significantly when it is >FMQ (Lee et al., 2005) (Fig. 6). Therefore, the degrees of partial melting of the mantle should be considered when the V/Sc ratio of primary magma is used to calculate mantle fO_2. Mafic magmas in subduction zones are generally produced by higher degrees of partial melting of the mantle (*e.g.*, up to 15-20%, Kelley et al., 2006) than those in the mid-ocean ridges (~10%, Bottinga and Allegre, 1976). The degrees of partial melting of the mantle are thus set to be 15 to 20% for the intrusions in the CAOB, the obtained mantle fO_2 of the Heishan, Huangshannan, Luodong, Poyi and Hongqiling No.2 intrusions is ~FMQ+1.0, ~FMQ, ~FMQ, ~FMQ+1.0 and ~FMQ+0.5, respectively (Fig. 6).

In our previous study, the mantle fO_2 of the Poyi and Hongqiling No.2 intrusions was estimated to be FMQ+0.3 and FMQ+0.5, respectively, using the olivine-spinel oxygen barometer (Cao et al., 2019). As the chemical data of the spinel from the Poyi intrusion in that study were collected from the literature and the $Fe^{3+}/\Sigma Fe$ of the spinel was not corrected, the obtained mantle fO_2 was likely underestimated by ~0.6 log unit (Cao et al., 2019), so the mantle fO_2 of the Poyi intrusion could be ~FMQ+0.9. Therefore, the mantle fO_2 of the Poyi and Hongqiling No.2 intrusions obtained by two different ways are quite consistent with each other.

Magma fO_2

The magma fO_2 of the mafic-ultramafic intrusions in the CAOB was acquired by two methods; one is based on the olivine-spinel oxygen barometer (Ballhaus et al., 1991), the other is based on V partitioning in olivine (Canil, 1997; Shishkina et al., 2018).

Olivine-spinel oxygen barometer. The oxygen fugacity of magmas was calculated using the olivine-spinel oxygen barometer given by Ballhaus et al. (1991):

$$log_{10}fO_2(\Delta QFM) = 0.27 + 2505/T - 400P/T - 6log\left(X_{Fe}^{Ol}\right) - 3200\left(1 - X_{Fe}^{Ol}\right)^2/T + 2\log\left(X_{Fe2+}^{Spl}\right) + 4\log(X_{Fe3+}^{Spl}) + 2630(X_{Al}^{Spl})^2/T \qquad (2)$$

where P is pressure in GPa, T is temperature in K, X_{Fe}^{Ol} is molar $Fe^{2+}/(Fe^{2+}+Mg^{2+})$ in olivine, X_{Fe3+}^{Spl} is molar $Fe^{3+}/\Sigma R^{3+}$ in spinel, X_{Al}^{Spl} is molar Al/ ΣR^{3+} in spinel, and X_{Fe2+}^{Spl} is molar $Fe^{2+}/(Fe^{2+}+Mg^{2+})$ in spinel. Olivine grains in the samples from the intrusions in the CAOB have Fo contents varying from 82 to 90, with most being >84 (Table S1), and those from the Dali picrite have Fo contents varying from 82 to 92 (Kamenetsky et al., 2012; Liu et al., 2017), which are all applicable to the equation. The pressure was calculated using the clinopyroxene geobarometer given by Nimis and Ulmer (1998) (Table S1). The $Fe^{3+}/\Sigma Fe$ of the spinel from the Jinbulake, Erbutu, Baixintan, Huangshannan and Tulaergen intrusions is corrected based on the EPMA data obtained in this study, whereas the $Fe^{3+}/\Sigma Fe$ of the spinel from the Heishan, Luodong intrusions and Dali picrite cannot be corrected as the EPMA data were collected from the literature. The magma fO_2 calculated using uncorrected $Fe^{3+}/\Sigma Fe$ of the spinel is 0.2 to 0.6 log units lower than that using corrected $Fe^{3+}/\Sigma Fe$ (Cao et al., 2019). However, the bias becomes smaller with increasing fO_2, which is <0.4 log units when fO_2 is >FMQ+1, and is <0.2 log units when fO_2 is >FMQ+1.5 (Cao et al., 2019).

The accuracy of the results depends on whether or not the olivine-spinel pairs in the rocks are in chemical equilibrium (Ballhaus et al., 1991). The spinel grains in this study overall are euhedral, fresh and homogeneous, and are commonly enclosed within olivine (Fig. S1c). The textures showing chemical disequilibrium, such as complex zoning, embayment, symplectite and sieve texture, are not observed in both minerals. In addition, the olivine-spinel pairs in the rocks from the intrusions in the CAOB overall have $ln\mathrm{Kd}_{\mathrm{Mg/Fe}}^{\mathrm{Ol\text{-}Spl}}$ positively correlated with XCr^{3+} [molar $Cr^{3+}/(Fe^{3+}+Cr^{3+}+Al^{3+})$] along the equilibrium lines between 600 and 700°C (Fig. 7), indicating that the olivine-spinel pairs reached chemical equilibrium. The temperatures of the equilibrium lines on Fig. 7 were estimated from the experimental data related to the reciprocal reaction ($FeCr_2O_4$ $+MgAl_2O_4$ = $MgCr_2O_4$ $+FeAl_2O_4$) in spinel (Liermann and Ganguly, 2003), which are consistent with the equilibrium temperatures calculated using the olivine-spinel thermometer given by Ballhaus et al. (1991) (Table S1). It is noted that the obtained temperature values are the closure temperatures of $Mg\text{-}Fe^{2+}$ diffusion between olivine and spinel on subsolidus cooling, which are lower than the crystallization temperature of minerals (Kamenetsky et al., 2001). However, the fO_2 could be only elevated by ~0.2 log units due to subsolidus $Mg\text{-}Fe^{2+}$ equilibrium between the olivine-spinel pairs (Birner et al., 2018). Therefore, the fO_2 values obtained using the closure temperatures of the olivine-spinel pairs can be taken as the magma fO_2 of the intrusions.

Using the equation 2, we obtained the magma fO_2 of the Jinbulake, Heishan, Erbutu, Baixintan, Huangshannan, Luodong and Tulaergen intrusions, which ranges from FMQ+1.2 to FMQ+2.6, FMQ+1.3 to FMQ+2.3, FMQ-0.1 to FMQ+1.2, FMQ+1.3 to FMQ+3.0, FMQ+0.6 to FMQ+2.6, FMQ+0.3 to FMQ+1.7, FMQ+2.5 to FMQ+2.9,

DOI: https://doi.org/10.2138/am-2020-7351. http://www.minsocam.org/

respectively (Table S1 and Fig. 8a). Although the values for the Heishan and Luodong intrusions were calculated using uncorrected $Fe^{3+}/\Sigma Fe$ of the spinel, the upper values should be reliable (*c.f.*, Cao et al., 2019). These data, together with the magma fO_2 of the Huangshandong, Huangshanxi, Poyi and Hongqiling No.1 and No.2 intrusions obtained in our earlier studies (Cao et al., 2019; Wei et al., 2019), display a negative correlation between the magma fO_2 and the Fo contents of olivine, except for the Erbutu intrusion (Fig. 8b).

The olivine-spinel pairs from the Dali picrite plot between the equilibrium lines at 900 and 1100°C (Fig. 7). The magma fO_2 of the Dali picrite varies from FMQ+0.2 to FMQ+0.8 (Fig. 8a). Given that the uncorrected $Fe^{3+}/\Sigma Fe$ of the spinel was used in the calculation, the results could be underestimated by ~0.6 log units in this case (*c.f.*, Cao et al., 2019). However, even if the bias is considered, the magma fO_2 of the Dali picrite is still much lower than the magma fO_2 of the mafic-ultramafic intrusions in the CAOB (Fig. 8a).

Vanadium partitioning in olivine ($\boldsymbol{D_{\mathrm{V}}^{\mathrm{Ol}}}$). Experimental results demonstrated that the partition coefficient of V between olivine and melt will decrease with elevating magma fO_2 (*e.g.,* Canil, 1997, 2002; Mallmann and O'Neill, 2013; Laubier et al., 2014; Shishkina et al., 2018). This relationship was used to calculate the magma fO_2 of hydrous arc basalts (Shishkina et al., 2018), *i.e.*,

$$\Delta \mathrm{FMQ} = -3.07 \times log D_v^{Ol} - 3.34 \qquad (3)$$

A common way to measure D_v^{Ol} is to acquire the V concentration of melt inclusion and host olivine in basalts. However, melt inclusions trapped in the olivine of cumulates are difficult to be found and analyzed as they are usually very small. We therefore chose an alternative protocol to estimate the D_v^{Ol} .

Vanadium and Sc are highly incompatible to olivine and have similar diffusion rates between olivine and trapped liquid in crystal mush (Locmelis et al., 2019), the V/Sc ratio of olivine is thus hardly affected by the trapped liquid shift effect. In addition, the V/Sc ratio of olivine is resistant to post-magmatic overprints, crustal contamination and crystallization of small amounts of spinel (<5%) (Lee et al., 2005; Locmelis et al., 2019). Nevertheless, we tried to analyze the core part of the best-preserved olivine grains in each sample to warrant that the primary V/Sc ratio of olivine is acquired. In theory, the V/Sc ratio of olivine can be calculated using the equation:

$$\left(\frac{\mathrm{V}}{\mathrm{Sc}}\right)_{Ol} = \frac{D_v^{Ol} \times V_{Liq}}{D_{Sc}^{Ol} \times Sc_{Liq}} \qquad (4)$$

Since D_{Sc}^{Ol} is constant at ~0.2 (Villemant et al., 1981; Sun and Liang, 2013), the equation 4 can be simplified as the equation:

$$\left(\frac{\mathrm{V}}{\mathrm{Sc}}\right)_{Ol} = \frac{D_v^{Ol} \times V_{Liq}}{0.2 \times Sc_{Liq}} \qquad (5)$$

D_V^{Ol} can be then acquired through the equation:

$$D_v^{Ol} = 0.2 \times \frac{\left(\frac{\mathrm{V}}{\mathrm{Sc}}\right)_{Ol}}{\left(\frac{\mathrm{V}}{\mathrm{Sc}}\right)_{Liq}} \qquad (6)$$

If equation 6 is combined with equation 3, the magma fO_2 can be calculated by the equation:

$$\Delta\mathrm{FMQ} = -3.07 \times log\left[0.2 \times \frac{\left(\frac{\mathrm{V}}{\mathrm{Sc}}\right)_{Ol}}{\left(\frac{\mathrm{V}}{\mathrm{Sc}}\right)_{Liq}}\right] - 3.34 \qquad (7)$$

Although V and Sc are highly incompatible to both olivine and orthopyroxene, Sc is more compatible to clinopyroxene than V (Canil, 2002). $(V/Sc)_{Liq}$ would vary slightly when olivine and/or orthopyroxene are on liquidus, but increase significantly when clinopyroxene is on liquidus during the fractionation of mafic magmas (Laubier et al., 2014). Most samples in this study contain olivine and/or orthopyroxene as major cumulus minerals (Fig. S1), except for those from the Jinbulake intrusion. Therefore, $(V/Sc)_{Liq}$ can be referred to the V/Sc ratio of the primary magma for each intrusion in the CAOB (Table S2), and then the magma fO_2 of the intrusions can be directly calculated using equation 7 (Table S3).

Comparison of the results based on the two methods. The obtained magma fO_2 values based on the two methods are consistent with each other within uncertainties (Fig. 9a). The V/Sc ratios of the olivine from the Erbutu, Huangshannan, Hongqiling No.1 and No.2 intrusions generally decrease with increasing magma fO_2 values that were obtained based on the olivine-spinel oxygen barometer (Fig. 9b), indicating that the obtained magma fO_2 values in this study is reliable (*c.f.*, Canil, 1997, 2002; Mallmann and O'Neill, 2013; Laubier et al., 2014; Shishkina et al., 2018).

In summary, the magma fO_2 values of the arc-hosted Jinbulake and Heishan intrusions are comparable to those of the post-collisional Baixintan, Huangshandong, Huangshanxi, Huangshannan, Tulaergen, Hongqiling No.1 and No.2 intrusions. The magma fO_2 values of the mafic-ultramafic intrusions in the CAOB overall have a range similar to those of arc basalts (FMQ+0.5 to FMQ+6; Woodland et al., 2006), much higher than those of MORBs (FMQ-1 to FMQ+0.5; Cottrell and Kelley, 2011; Zhang et al., 2018) (Fig. 8a). The magma fO_2 values of the Erbutu, Poyi and Luodong intrusions

DOI: https://doi.org/10.2138/am-2020-7351. http://www.minsocam.org/

are lower than that of other intrusions in the CAOB, and overlap the upper fO_2 limit of MORBs (Fig. 8a). In contrast, the magma fO_2 values of the Dali picrite are basically within the range of MORBs (Fig. 8a).

DISCUSSIONS

The magma fO_2 of mafic-ultramafic intrusions in convergent margin settings could be controlled by complex factors such as the oxidation and fertility states of the metasomatized mantle sources (*e.g.*, Rielli et al., 2017), and magmatic processes (*e.g.*, Lee et al., 2005). In this study, our results indicate that metasomatized mantle sources of the mafic-ultramafic intrusions in the CAOB overall are slightly oxidized compared with that of MORBs, and the elevated magma fO_2 of the intrusions in both arc and post-subduction, extensional settings is mainly attributed to the fractionation of hydrated magmas derived from the metasomatized mantle.

Mantle fO_2 of the mafic-ultramafic intrusions in the CAOB

The arc-related Heishan intrusion and post-collisional Huangshannan, Poyi, Luodong and Hongqiling No.2 intrusions have mantle fO_2 ranging from ~FMQ to ~FMQ+1.0 (Fig. 6), slightly higher than the mantle fO_2 (≤ FMQ) of MORBs (Frost and McCammon, 2008; Kelley and Cottrell, 2009, 2012; Rielli et al., 2018a), but much lower than the mantle fO_2 of arc basalts (FMQ+1 to FMQ+4, Woodland et al., 2006). These results indicate that the mantle sources of mafic-ultramafic intrusions in the CAOB are not highly oxidized as supposed for the subarc mantle. In addition, the mantle fO_2 is much lower than the magma fO_2 of these intrusions (Fig. 8b), the high magma fO_2 of the intrusions in the CAOB is thus not governed by the oxidation state of the mantle source alone.

The oxidation of the subarc mantle is attributed to the transportation of highly oxidized, CO_3^{2-}-, SO_4^{2-}-, or Fe^{3+}-rich fluids to the subarc mantle during subduction (Mungall, 2002; Evans, 2006; Evans et al., 2012; Debret et al., 2016; Pons et al., 2016; Debret and Sverjensky, 2017; Rielli et al., 2017). However, this process is dependent on the subduction depth and temperature (Tomkins and Evans, 2015). Modeling results indicate that sulfate tends to be released at shallower subduction zone and relatively low temperatures, whereas sulfide tends to be released at deeper subduction zone and relatively high temperatures (Tomkins and Evans, 2015). The mafic-ultramafic intrusions in the CAOB are considered to have been derived from partial melts of the mantle wedge in the spinel stability field (*e.g.*, Zhang et al., 2016). It is likely that only minor slab-derived, oxidized components was involved in the mantle wedge at this depth. In addition, the mantle sources of these intrusions in the CAOB are considered to have experienced the interaction of the depleted lithospheric mantle with upwelling asthenospheric materials due to slab break-off (Han et al., 2010; Li et al., 2012; Xie et al., 2012; Wei et al., 2013; Mao et al., 2014, 2016; Deng et al., 2015). This process may also dilute the oxidized components in the mantle wedge because asthenospheric materials are typically more reduced than the lithospheric mantle by ~1 log unit (Wood et al., 1990). Therefore, the mafic-ultramafic intrusions in the CAOB overall have mantle fO_2 slightly higher than that for the mantle of MORBs.

Fractionation of hydrated magmas derived from metasomatized mantle sources

Experimental results indicate that the fractionation of olivine and clinopyroxene may slightly increase the $Fe^{3+}/\sum Fe$ of magmas and have a limited effect on the oxidization states of magmas (Cottrell and Kelley, 2011; Kelley and Cottrell, 2012). However, water

DOI: https://doi.org/10.2138/am-2020-7351. http://www.minsocam.org/

in silicate magmas can play an efficient ‘catalyst’ to promote the oxidation states of magmas if it is partially dissociated and loss H^+ at high temperatures (Carmichael, 1991; Cornejo and Mahood, 1997), or exsolved from the melt that carried more Fe^{2+} than Fe^{3+} (Bell and Simon, 2011). Mafic magmas tend to become more hydrous with fractionation because volatiles (*e.g.*, H_2O) are essentially incompatible to olivine and clinopyroxene. Therefore, the fractionation process could significantly elevate the oxidation states of hydrated, mafic magmas.

The mafic-ultramafic intrusions in the CAOB contain abundant hydrous minerals such as amphibole and phlogopite (*e.g.,* Deng et al., 2014; Su et al., 2011; Xie et al., 2012; Wei et al., 2013, 2015). On the plot of Alz versus TiO_2, the clinopyroxene from the intrusions in the CAOB has Alz/Ti scattered along the arc cumulate trend, in contrast to the low Alz/Ti of the clinopyroxene from the sulfide-bearing mafic-ultramafic intrusions in the Emeishan LIP (Fig. 10). The high Alz values of the clinopyroxene from the CAOB are attributed to the idea that more Al would enter the tetrahedral site of clinopyroxene with increasing H_2O content of melt (*c.f.*, Loucks, 1990). This is consistent with an interpretation that the parental magmas of the intrusions in the CAOB may be hydrated due to the derivation from the mantle sources metasomatized by slab-derived melts/fluids. There is an overall negative correlation between the magma fO_2 and the Fo contents of olivine for the intrusions in the CAOB (Fig. 8b), showing that the magmas became more oxidized with fractionation. Therefore, the H_2O content of magmas derived from the metasomatized mantle and relative degrees of the fractionation of magmas are likely two key factors controlling magma fO_2 of the mafic-ultramafic intrusions in convergent margin settings.

The Erbutu intrusion is an exceptive case as the olivine grains of the intrusion have Fo contents comparable with those for the olivine of the Jinbulake and Heishan intrusions, but the intrusion has much lower magma fO_2 than the latter two intrusions (Fig. 8b). The parental magma of the Erbutu intrusion is thought to be boninitic that may have been emplaced early in the subduction history (*c.f.*, Jian et al., 2010; Peng et al., 2013). As the oxidation of the mantle wedge by the metasomatizing agents could occur after subduction initiation in 1 Myr. (*c.f.*, Brounce et al., 2015), it is likely that the mantle source of the Erbutu intrusion is relatively reduced, thus the magma fO_2 of this intrusion is lower than that of other intrusions in the CAOB for a given degree of fractionation of magma.

Magma fO_2 constraints for Ni-Cu sulfide mineralization in convergent margin settings

Experimental results show that the sulfur solubility of silicate magma could increase by an order of magnitude if the magma fO_2 increases from FMQ+0.5 to FMQ+1.5 (Luhr, 1990; Jugo et al., 2005; Jugo, 2009; Jugo et al., 2010). The mantle-derived mafic magmas in intraplate settings usually have magma fO_2 ranging from FMQ-1 to FMQ+0.5 and could dissolve a maximum of ~1500 ppm S (*c.f.*, Wood et al., 1990; Jugo et al., 2010), therefore the formation of economic Ni-Cu sulfide deposits often requires the addition of external crustal sulfur into the magmas (*e.g.*, Li et al., 2001; Ripley and Li, 2003; Barnes and Lightfoot, 2005; Wang et al., 2006; Mungall and Naldrett, 2008; Keays and Lightfoot, 2010; Taranovic et al., 2018). For instance, the Ni-Cu sulfide deposits in the Emeishan LIP and the Jinchuan Ni-Cu deposit formed in a rifting setting have magma fO_2 overlapping with the range of MORBs, and the sulfides from the deposits have highly variable δ^{34}S (-4 to +8‰, Fig. 11), indicating substantial addition of external crustal sulfur in the formation of these deposits (Ripley et al., 2005; Duan et al., 2016; Wang et al., 2018).

In contrast, the mantle-derived mafic magmas in convergent margin settings have fO_2 ranging from FMQ+0.5 to FMQ+3 (Fig. 8a) and could dissolve ~1800 to ~13,000 ppm S (Jugo et al., 2010), much higher than the S solubility of the magmas in intraplate settings. In addition, the sulfides from the Ni-Cu sulfide-bearing mafic-ultramafic intrusions in the post-subduction, extensional setting in the CAOB have δ^{34}S values (-1.0 to +1.3‰) nearly identical to that of the MORB mantle (Fig. 11), despite the large δ^{34}S range (-10.0 to +5.4‰) of the sulfides from the metasomatized mantle xenoliths (Rielli et al., 2018b). This was interpreted as the magmas of the Ni-Cu sulfide-bearing mafic-ultramafic intrusions in the CAOB contain dominantly mantle-derived sulfur with trivial addition of external crustal sulfur (Wei et al., 2019). Therefore, the high magma fO_2 and the MORB mantle-like δ^{34}S of the mafic-ultramafic intrusion in the CAOB indicate that highly oxidized, mantle-derived magmas may be capable of dissolving enough mantle-derived sulfur to form magmatic Ni-Cu sulfide deposits so that the addition of external crustal sulfur is not always necessary in such cases. In addition, the mafic-ultramafic intrusions in the CAOB that have sulfides with mantle-like δ^{34}S values generally have magma fO_2>FMQ+1, whereas the Erbutu intrusion that has sulfides with the highest δ^{34}S values has magma fO_2<FMQ+1 (Fig. 11), we thus consider that the mantle-derived mafic magmas with fO_2 greater than ~FMQ+1.0 may be able to dissolve sufficient mantle-derived sulfur to form important Ni-Cu sulfide deposits in convergent margin settings (*c.f.,* Rielli et al., 2018a).

On the other hand, the formation of economic Ni-Cu sulfide deposits from the highly oxidized, mantle-derived magmas depends on how the magmas can be reduced to reach sulfide saturation so that the sulfide melts can be segregated from the magmas (Tomkins et al., 2012). This can be examined by comparing the fO_2 between the parental magmas prior to sulfide saturation and the magmas concurrent with sulfide saturation (*e.g.,* Wei et al., 2019). The magma fO_2 obtained by the olivine-spinel oxygen barometer in this study can represent the parental magma fO_2 before sulfide saturation. The fO_2 of the magmas concurrent with sulfide saturation for the intrusions in the CAOB were estimated using Fe-Ni exchange between olivine and sulfide liquid (*e.g.*, Feng et al., 2017; Mao et al., 2018; Wei et al., 2019). As shown in Fig. 12, the magma fO_2 at sulfide saturation is considerably lower than the fO_2 of parental magmas for each intrusion, indicating that the oxidized magmas was indeed reduced with the sulfide saturation of magmas. A possible way to trigger the reduction is the crystallization of magnetite (Jenner et al., 2010). However, this mechanism does not appear as the driver of magma reduction in the CAOB because the examined rocks in this study contain few magnetite. Alternatively, the reduction of oxidized magmas can be triggered by the addition of organic-carbon or graphite-rich sedimentary rocks, which was evidenced by the C isotope studies on a few intrusions in the CAOB (*e.g.,* Wei et al., 2019) and the O isotope studies of the olivine in the lower zone of the Huangshanxi intrusion (Mao et al., 2019).

IMPLICATIONS

Most Ni-Cu sulfide-bearing mafic-ultramafic intrusions in the CAOB have magma fO_2 (FMQ+0.5 to FMQ+3) much higher than that of MORBs (FMQ-1 to FMQ+0.5), consistent with the global observation that the mafic-ultramafic intrusions emplaced in convergent margin settings have relatively high magma fO_2. In contrast, the mantle fO_2 of these intrusions ranges from FMQ to ~FMQ+1.0, just slightly higher than that of MORBs (≤ FMQ). Because the amounts of oxidized components that were added to the metasomatized mantle wedges generally decrease with the depth of the mantle wedges in convergent margin settings, the slightly oxidized mantle source of the intrusions in the CAOB is likely related to the limited amounts of slab-derived, oxidized components added to mantle wedges and relatively deep mantle wedges where the partial melting occurred. The negative correlation of the magma fO_2 and the Fo contents of the olivine of the intrusions in the CAOB indicates that the magma fO_2 could be elevated with the fractionation of hydrated, mafic magmas derived from metasomatized mantle sources. In addition, the mafic-ultramafic intrusions that host economic Ni-Cu sulfide deposits in the CAOB usually have sulfides with mantle-like $\delta^{34}S$ (-1.0 to +1.1‰) and magma fO_2>FMQ+1, indicating that the relatively oxidized magmas may be capable of dissolving enough mantle-derived sulfur to form economic Ni-Cu sulfide deposits in convergent margin settings. The sulfide saturation of the oxidized, mafic magmas may be triggered by the addition of organic-carbon or graphite-rich sedimentary rocks into the magmas. Therefore, our results imply that the addition of external crustal sulfur is not so compulsory to trigger the sulfide saturation of highly oxidized, mantle-derived mafic magmas and the formation of economic Ni-Cu sulfide deposits in convergent margin settings, although it is very important in the formation of giant Ni-Cu sulfide deposits such as those at Noril'sk in Russia (Ripley and Li, 2013).

ACKNOWLEDGEMENTS AND FUNDING

This work was supported by grants from the National Natural Science Foundation of China (No. 41730423 and 41902077), and China Postdoctoral Science Foundation Grant (No. 2019M653103). Shenghong Yang provided the samples of the Jinbulake intrusion and Benxun Su shared the EPMA data for the olivine and spinel of the Luodong intrusion. Constructive reviews by Andrew Tomkins and an anonymous reviewer have greatly improved the quality of this manuscript.

REFERENCES

Ballhaus C., Berry R.F., and Green D.H. (1991) High pressure experimental calibration of the olivine-orthopyroxene-spinel oxygen geobarometer: implications for the oxidation state of the upper mantle. Contributions to Mineralogy and Petrology 107, 27–40.

Barnes S-.J., and Lightfoot P.C. (2005) Formation of magmatic nickel-sulfide ore deposits and processes affecting their copper and platinum-group element contents. In Economic Geology 100th Anniversary Volume (eds. J. W. Hedenquist, J. H. Thompson, R. J. Goldfarb and J. P. Richards). pp. 179-213.

Bell A.S., and Simon A. (2011) Experimental evidence for the alteration of the $Fe^{3+}/\Sigma Fe$ of silicate melt caused by the degassing of chlorine-bearing aqueous volatiles. Geology 39, 499–502.

Bénard A., Woodland A.B., Arculus R.J., Nebel O., and McAlpine S.R.B. (2018) Variation in sub-arc mantle oxygen fugacity during partial melting recorded in refractory peridotite xenoliths from the West Bismarck Arc. Chemical Geology 486, 16–30.

Birner A., Cottrell E., Warren J.M., Kelley K.A., Davis F.A. (2018) Peridotites and basalts reveal broad congruence between two independent records of mantle fO_2 despite local redox heterogeneity. Earth and Planetary Science Letters 494, 172-189.

Bottinga Y., and Allegre C. (1976). Geophysical, petrological and geochemical models of the oceanic lithosphere. Tectonophysics 32, 9–59.

Brounce M., Kelley K.A., Cottrell E. and Reagan M.K. (2015) Temporal evolution of mantle wedge oxygen fugacity during subduction initiation. Geology 43, 775–778.

Brounce M., Stolper E., and Eiler J. (2017) Redox variations in Mauna Kea lavas, the oxygen fugacity of the Hawaiian plume, and the role of volcanic gases in Earth's oxygenation. PNAS 114, 8997–9002.

Canil D. (1997) Vanadium partitioning and the oxidation state of Archean komatiite magmas. Nature 389, 842-845.

Canil D. (2002) Vanadium in peridotites, mantle redox and tectonic environments: Archean to present. Earth and Planetary Science Letters 195, 75-90.

Canil D., and Fedortchouk Y. (2001) Olivine-liquid partitioning of vanadium and other trace elements, with applications to modern and ancient picrites. The Canadian Mineralogist 39, 319-330.

Cao Y., Wang C.Y., and Wei B. (2019) Magma oxygen fugacity of Permian to Triassic Ni-Cu sulfide-bearing mafic-ultramafic intrusions in the central Asian orogenic belt, North China. Journal of Asian Earth Sciences 173, 250–262.

Carmichael I.S.E. (1991) The redox states of basic and silicic magmas- a reflection of their source regions. Contributions to Mineralogy and Petrology 106, 129–141.

Cornejo P.C., and Mahood G.A. (1997) Seeing past the effects of re-equilibration to reconstruct magmatic gradients in plutons: La Gloria Pluton, central Chilean Andes. Contributions to Mineralogy and Petrology 127, 159–175.

Cottrell E., and Kelley K.A. (2011) The oxidation state of Fe in MORB glasses and the oxygen fugacity of the upper mantle. Earth and Planetary Science Letters 305, 270–282.

Dauphas N., Teng F.-Z., and Arndt N.T. (2010) Magnesium and iron isotopes in 2.7 Ga Alexo komatiites: Mantle signatures, no evidence for Soret diffusion, and identification of diffusive transport in zoned olivine. Geochimica et Cosmochimica Acta 74, 3274–3291.

Debret B., and Sverjensky D.A. (2017) Highly oxidising fluids generated during serpentinite breakdown in subduction zones. Scientific Report 1–6.

Debret B., Millet M.-A., Pons M.-L., Bouilhol P., Inglis E., and Williams H. (2016) Isotopic evidence for iron mobility during subduction. Geology 44, 215-218.

Deng Y.F., Song X.Y., Chen L., Zhou T., Pirajno F., Yuan F., Xie W., and Zhang D. (2014) Geochemistry of the Huangshandong Ni-Cu deposit in northwestern China: Implications for the formation of magmatic sulfide mineralization in orogenic belts. Ore Geology Reviews 56, 181–198.

Deng Y.F., Song X.Y., Hollings P., Zhou T.F., Yuan F., and Zhang D. (2015) Role of asthenosphere and lithosphere in the genesis of the Early Permian Huangshan mafic-ultramafic intrusion in the Northern Tianshan, NW China. Lithos 227, 241–254.

Duan J., Li C., Qian Z., Jiao J., Ripley E.M., and Feng Y. (2016) Multiple S isotopes, zircon Hf isotopes, whole-rock Sr-Nd isotopes, and spatial variations of PGE tenors in the Jinchuan Ni-Cu-PGE deposit, NW China. Mineralium Deposita 51, 557–574.

Evans B.W., Dyar M.D., and Kuehner S.M. (2012) Implications of ferrous and ferric iron in antigorite. American Mineralogist 97, 184–196.

Evans K.A. (2006) Redox decoupling and redox budgets: Conceptual tools for the study of earth systems. Geology 34, 489-492.

Feng Y., Qian Z., Xu G., Duan J., Chen B., Sun T., Jiang C., and Ren M. (2017) Rock-forming mineral features of Permian mineralized mafic-ultramafic intrusions in East Tianshan Mountains and their implications for intrusion generation. Acta Petrological et Mineralogical 36, 519-534 (in Chinese with English abstract).

Frost D.J., and McCammon C.A. (2008) The redox state of earth's mantle. Annual Review of Earth and Planetary Science 389-420.

Gaillard F., Scaillet B., Pichavant M., and Lacono-Marziano G. (2015) The redox geodynamics linking basalts and their mantle sources through space and time. Chemical Geology 418, 217–233.

Gao J.-F., Zhou M.-F., Lightfoot P., and Qu W. (2012) Heterogeneous Os isotope compositions in the Kalatongke sulfide deposit, NW China: the role of crustal contamination. Mineralium Deposita 47, 731−738.

Godel B., Barnes S.J., and Maier W. D. (2011) Parental magma composition inferred from trace element in cumulus and intercumulus silicate minerals: an example from the lower and lower critical zones of the Bushveld Complex, South-Africa. Lithos 125, 537–552.

Han C., Xiao W., Zhao G., Ao S., Zhang J., Qu W., and Du A. (2010) In-situ U-Pb, Hf and Re-Os isotopic analyses of the Xiangshan Ni-Cu- Co deposit in Eastern Tianshan (Xinjiang), Central Asia Orogenic Belt: Constraints on the timing and genesis of the mineralization. Lithos 120, 547–562.

Han C., Xiao W., Zhao G., Qu W., and Du A. (2007) Re–Os dating of the Kalatongke Cu–Ni deposit, Altay Shan, NW China, and resulting geodynamic implications. Ore Geology Reviews 32, 452–468.

Hao L., Zhao X., Boorder H.D., Lu J., Zhao, Y., and Wei, Q. (2014) Origin of PGE depletion of Triassic magmatic Cu-Ni sulfide deposits in the central-southern area of Jilin province, NE China. Ore Geology Reviews 63, 226–237.

Ionov D.A., and Wood B.J. (1992) The oxidation state of subcontinental mantle: oxygen thermobarometry of mantle xenoliths from central Asia. Contributions to Mineralogy and Petrology 111, 179–193.

Jahn B.M., Windley B., Natal'in B., and Dobretsov N. (2004) Phanerozoic continental growth in Central Asia. Journal of Asian Earth Sciences 23, 599-603.

Jahn B.M., Wu F.Y., and Chen B. (2000) Massive granitoid generation in Central Asia: Nd isotope evidence and implication for continental growth in the Phanerozoic. Episodes 23, 82–92.

Jenner F.E., O'Neill H.St.C., Arculus R.J., and Mavrogenes J.A. (2010) The magnetite crisis in the evolution of arc-related magmas and the initial concentration of Au, Ag and Cu. Journal of Petrology 51, 2445–2464.

Jian P., Liu D., Kröner A., Windley B.F., Shi Y., Zhang W., Zhang F., Miao L., Zhang L., and Tomurhuu D. (2010) Evolution of a Permian intraoceanic arc–trench system in the Solonker suture zone, Central Asian Orogenic Belt, China and Mongolia. Lithos 118, 169-190.

Jiang Y.-H., Jiang S.-Y., Dai B.-Z., Liao S.-Y., Zhao K.-D., and Ling H.-F. (2009) Middle to late Jurassic felsic and mafic magmatism in southern Hunan Province, southeast China: Implications for a continental arc to rifting. Lithos 107, 185–204.

Jugo P.J. (2009) Sulfur content at sulfide saturation in oxidized magmas. Geology 37, 415–418.

Jugo P.J., Luth R.W., and Richards J.P. (2005) Experimental data on the speciation of sulfur as a function of oxygen fugacity in basaltic melts. Geochimica et Cosmochimica Acta 69, 497–503.

Jugo P.J., Wilke M., and Botcharnikov R.E. (2010) Sulfur K-edge XANES analysis of natural and synthetic basaltic glasses: Implications for S speciation and S content as function of oxygen fugacity. Geochimica et Cosmochimica Acta 74, 5926–5938.

Kamenetsky V.S., Chung S.-L., Kamenetsky M.B., and Kuzmin D.V. (2012) Picrites from the Emeishan large igneous province, SW China: a compositional continuum in primitive magmas and their respective mantle sources. Journal of Petrology 53, 2095-2113.

Kamenetsky V.S., Crawford A.J., and Meffre S. (2001) Factors controlling chemistry of magmatic spinel: An empirical study of associated olivine, Cr-spinel and melt inclusions from primitive rocks. Journal of Petrology 42, 655–671.

Keays R.R., and Lightfoot P.C. (2010) Crustal sulfur is required to form magmatic Ni–Cu sulphide deposits; evidence from chalcophile element signatures of Siberian and Deccan Trap basalts. Mineralium Deposita 45, 241–257

Kelley K.A., and Cottrell E. (2009) Water and the oxidation state of Subduction Zone Magmas. Science 325, 605–607.

Kelley K.A., and Cottrell E. (2012) The influence of magmatic differentiation on the oxidation state of Fe in a basaltic arc magma. Earth and Planetary Science Letters 329–330, 109–121.

Kelley K.A., Plank T., Grove T.L., Stolper E.M., Newman S., and Hauri E. (2006). Mantle melting as a function of water content beneath back-arc basins. Journal of Geophysical Research: Solid Earth 111, B09208.

Kelley K.A., Plank T., Newman S., Stolper E., Grove T.L., Parman S., and Hauri E. (2010) Mantle melting as a function of water content beneath the Mariana arc. Journal of Petrology 51, 1711–1738.

Kress V.C., and Carmichael I.S.E. (1991) The compressibility of silicate liquids containing Fe_2O_3 and the effect of composition, temperature, oxygen fugacity and pressure on their redox states. Contributions to Mineralogy and Petrology108, 82–92

Labidi J., Cartigny P., and Moreira M. (2013) Non-chondritic sulphur isotope composition of the terrestrial mantle. Nature 501, 208–211.

Labidi J., Cartigny P., Hamelin C., Moreira M., and Dosso L. (2014) Sulfur isotope budget (^{32}S, ^{33}S, ^{34}S and ^{36}S) in Pacific-Antarctic Ridge basalts; a record of mantle source heterogeneity and hydrothermal sulfide assimilation. Geochimica et Cosmochimica Acta133, 47–67.

Laubier M., Grove T.L., and Langmuir C.H. (2014) Trace element mineral/melt partitioning for basaltic and basaltic andesitic melts: An experimental and laser ICP-MS study with application to the oxidation state of mantle source regions. Earth and Planetary Science Letters 392, 265–278.

Lee C.T.A., Leeman W.P., Canil D., and Li Z.X.A. (2005) Similar V/Sc systematics in MORB and arc basalts: Implications for the oxygen fugacities of their mantle source regions. Journal of Petrology 46, 2313–2336.

Lee C.T.A., Luffi P., Le Roux V., Dasgupta R., Albaréde F., and Leeman W.P. (2010) The redox state of arc mantle using Zn/Fe systematics. Nature 468, 681–685.

Li C., and Ripley E.M. (2011) The giant Jinchuan Ni-Cu-(PGE) deposit; tectonic setting, magma evolution, ore genesis, and exploration implications. Reviews in Economic Geology 17, 163–180.

Li C., Maier W.D., and Waal S.A. (2001) Magmatic Ni-Cu versus PGE deposits: contrasting genetic controls and exploration implication. South African Journal of Geology 104, 205–214.

Li C., Zhang M.J., Fu P., Qian Z.Z., Hu P.Q., and Ripley E.M. (2012) The Kalatongke magmatic Ni-Cu deposits in the Central Asian Orogenic Belt, NW China: product of slab window magmatism? Mineralium Deposita 47, 51–67.

Li C., Zhang Z., Li W., Wang Y., Sun T., and Ripley E.M. (2015) Geochronology, petrology and Hf-S isotope geochemistry of the newly-discovered Xiarihamu magmatic Ni-Cu sulfide deposit in the Qinghai-Tibet plateau, western China. Lithos 216, 224–240.

Li J.L., Schwarzenbach E.M., John T., Ague J.J., Huang F., Gao, J., Klemd R., Whitehouse M.J., and Wang X.S. (2020) Uncovering and quantifying the subduction zone sulfur cycle from the slab perspective. Nature Communications 11, 1-12.

Li Y. (2018) Temperature and pressure effects on the partitioning of V and Sc between clinopyroxene and silicate melt: Implications for mantle oxygen fugacity. American Mineralogist 103, 819–823.

Liermann H.P., and Ganguly J. (2003) Fe^{2+}-Mg fractionation between orthopyroxene and spinel: experimental calibration in the system FeO–MgO–Al_2O_3–Cr_2O_3–SiO_2, and applications. Contributions to Mineralogy and Petrology 154, 217–227.

Liu J., Xia Q.-K., Kuritani T., Hanski E., and Yu H.-R. (2017) Mantle hydration and the role of water in the generation of large igneous provinces. Nature Communication 8, 1824.

Locmelis M., Arevalo R.D., Puchtel I.S., Fiorentini M.L., and Nisbet E.G. (2019) Transition metals in komatiitic olivine: Proxies for mantle composition, redox conditions, and sulfide mineralization potential. American Mineralogist 104, 1143–1155.

Loucks R.R. (1990) Discrimination from opholitic and nonopholitic ultramafic–mafic allochthons in orogenic belts by the Al/Ti ratios in clinopyroxene. Geology 18, 346–349.

Luhr J.F. (1990) Experimental phase relations of water- and sulfur-saturated arc magmas and the 1982 eruptions of El Chichon volcano. Journal of Petrology 31, 1071–1114.

Maier W.D., Barnes S.J., Chinyepi G., Barton J.J., Eglington B., and Setshedi T. (2008) The composition of magmatic Ni-Cu-(PGE) sulfide deposits in the Tati and Selebi-Phikwe belts of eastern Botswana. Mineralium Deposita 43, 37-60.

Mallmann G., and O'Neill H.S.C. (2009) The crystal/melt partitioning of V during mantle melting as a function of oxygen fugacity compared with some other elements (Al, P, Ca, Sc, Ti, Cr, Fe, Ga, Y, Zr and Nb). Journal of Petrology 50, 1765–1794.

Mallmann G., and O'Neill H.S.C. (2013) Calibration of an empirical thermometer and oxybarometer based on the partitioning of Sc, Y and V between olivine and silicate melt. Journal of Petrology 54, 933–949.

Manor M.J., Scoates J.S., Nixon G.T., and Ames D.E. (2016) The giant mascot Ni-Cu-PGE deposit, British Columbia: mineralized conduits in a convergent margin tectonic setting. Economic Geology 111, 57–87.

Mao Y., Qin K., Barnes S. J., Ferraina C., Iacono–Marziano G., Verrall M., Tang D., and Xue S. (2018) A revised oxygen barometry in sulfide-saturated magmas and application to the Permian magmatic Ni–Cu deposits in the southern Central Asian Orogenic Belt. Mineralium Deposita 53, 731-755.

Mao Y., Qin K., Li C., and Tang D. (2015) A modified genetic model for the Huangshandong magmatic sulfide deposit in the Central Asian Orogenic Belt, Xinjiang, western China. Mineralium Deposita 50, 65–82.

Mao Y., Qin K., Li C., Xue S., and Ripley E.M. (2014) Petrogenesis and ore genesis of the Permian Huangshanxi sulfide ore-bearing mafic-ultramafic intrusion in the Central Asian Orogenic Belt, western China. Lithos 200–201, 111–125.

Mao Y., Qin K., Tang D., Feng H. and Xue S. (2016) Crustal contamination and sulfide immiscibility history of the Permian Huangshannan magmatic Ni-Cu sulfide deposit, East Tianshan, NW China. Journal of Asian Earth Sciences 129, 22–37.

Mao Y.J., Barnes S.J., Qin K.Z., Tang D., Martin L., Su B., and Evans N.J. (2019) Rapid orthopyroxene growth induced by silica assimilation: constraints from sector-zoned orthopyroxene, olivine oxygen isotopes and trace element variations in the Huangshanxi Ni–Cu deposit, Northwest China. Contributions to Mineralogy and Petrology 174, 1–24.

Mungall J. E. (2002) Roasting the mantle: Slab melting and the genesis of major Au and Au-rich Cu deposits. Geology 30, 915-918.

Mungall J.E., and Naldrett A.J. (2008) Ore Deposits of the Platinum-Group Elements. Element 4, 253–258.

Naldrett A.J. (2004) Magmatic sulfide deposits: geology, geochemistry and exploration. Springer, New York.

Nilsson K., and Peach C.L. (1993) Sulfur speciation, oxidation state and sulfur concentration in backarc magmas. Geochimica et Cosmochimica Acta 57, 3807–3813.

Nimis P., and Ulmer P. (1998) Clinopyroxene geobarometry of magmatic rocks Part 1: An expanded structural geobarometer for anhydrous and hydrous, basic and ultrabasic systems. Contributions to Mineralogy and Petrology 133, 122–135.

Peng R., Zhai Y., Li C., and Ripley M. (2013) The Erbutu Ni-Cu deposit in the Central Asian Orogenic Belt: A Permian Magmatic Sulfide deposit related to boninitic magmatism in an arc setting. Economic Geology 108, 1879-1888.

Pons M.-L., Debret B., Bouilhol P., Delacour A., and Williams H. (2016) Zinc isotope evidence for sulfate-rich fluid transfer across subduction zones. Nature Communication 7, 13794.

Qin K.Z., Su B.X., Li X.H., Tang D.M., Sakyi P.A., Sun H., Xiao Q.H., and Liu P.P. (2011). SIMS zircon U-Pb geochronology and Sr-Nd isotopes of mafic-ultramafic intrusions in eastern Tianshan and Beishan in correlation with flood basalts in Tarim basin (NW China): Constraints on a 280 Ma mantle plume. American Journal of Sciences 29, 275–289.

Rielli A., Tomkins A.G., Nebel O., Brugger J., Etschmann B., and Paterson D. (2018a) Garnet peridotites reveal spatial and temporal changes in the oxidation potential of subduction. Scientific Reports 8, 16411.

Rielli A., Tomkins A.G., Nebel O., Brugger J., Etschmann B., Zhong R., Yaxley G.M., and Paterson D. (2017) Evidence of sub-arc mantle oxidation by sulphur and carbon. Geochemical Perspective Letters 124–132.

Rielli A., Tomkins A.G., Nebel O., Raveggi M., Jeon H., Martin L., and Ávila J.N. (2018b) Sulfur isotope and PGE systematics of metasomatised mantle wedge. Earth and Planetary Science Letters 497, 181–192.

Ripley E.M., and Li C. (2003) Sulfur isotope exchange and metal enrichment in the formation of magmatic Cu-Ni-(PGE) deposits. Economic Geology 99, 635–641.

Ripley E.M., and Li, C. (2013) Sulfide saturation in mafic magmas: Is external sulfur required for magmatic Ni-Cu-(PGE) ore genesis? Economic Geology 108, 45-58.

Ripley E.M., Sarkar A., and Li C. (2005) Mineralogical and stable isotope studies of hydrothermal alteration at the Jinchuan Ni-Cu deposit. Economic Geology 100, 1349–1361.

Sengör A.C.A., Natal'in B.A., and Burtmann V.S. (1993) Evolution of the Altaid tectonic collage and Palaeozoic crustal growth in Eurasia. Nature 364, 299–306.

Shishkina T.A., Portnyagin M.V., Botcharnikov R.E., Almeev R.R., Simonyan A.V., Garbe-Schönberg D., Schuth S., Oeser M., and Holtz F. (2018) Experimental

DOI: https://doi.org/10.2138/am-2020-7351. http://www.minsocam.org/

Calibration and Implications of Olivine-Melt Vanadium Oxybarometry for Hydrous Basaltic Arc Magmas. American Mineralogist 103, 369–383.

Song X.-Y., and Li X.-R. (2009) Geochemistry of the Kalatongke Ni-Cu- (PGE) sulfide deposit, NW China: Implications for the formation of magmatic sulfide mineralization in a postcollisional environment. Mineralium Deposita 44, 303–327.

Song X.-Y., Chen L.-M., Deng Y.-F., and Xie W. (2013) Syncollisional tholeiitic magmatism induced by asthenosphere upwelling owing to slab detachment at the southern margin of the Central Asian orogenic belt. Journal of Geological Society 170, 941–950.

Song X.-Y., Yi J., Chen L., She Y., Liu C., Dang X.F., Yang Q., and Wu S. (2016) The Giant Xiarihamu Ni-Co sulfide deposit in the East Kunlun Orogenic Belt, Northern Tibet Plateau. China. Economic Geology 111, 29–55.

Su B.X., Qin K.Z., Lu Y., Sun H., and Sakyi P.A. (2015) Decoupling of whole-rock Nd-Hf and zircon Hf-O isotopic compositions of a 284 Ma mafic-ultramafic intrusion in the Beishan Terrane, NW China. International Journal of Earth Sciences 104, 1721-1737.

Su B.X., Qin K.Z., Sakyi P.A., Li X.H., Yang Y.H., Sun H., Tang D.M., Liu P.P., Xiao Q.H., and Malaviarachchi S.P.K. (2011) U–Pb ages and Hf-O isotopes of zircons from Late Paleozoic mafic–ultramafic units in the southern Central Asian Orogenic Belt: tectonic implications and evidence for an Early-Permian mantle plume. Gondwana Research 20, 516–531.

Sun C., and Liang Y. (2013) The importance of crystal chemistry on REE partitioning between mantle minerals (garnet, clinopyroxene, orthopyroxene, and olivine) and basaltic melts. Chemical Geology 358, 23–36.

Sun S.S., and McDonough W.F. (1989) Chemical and isotopic systematics of oceanic basalts: implications for mantle composition and processes. Geological Society, London, Special Publications 42, 313–345.

Sun T., Qian Z.-Z., Li C., Xia M.-Z., and Yang S.-H. (2013) Petrogenesis and economic potential of the Erhongwa mafic-ultramafic intrusion in the Central Asian Orogenic Belt, NW China: Constraints from olivine chemistry, U-Pb age and Hf isotopes of zircons, and whole-rock Sr-Nd-Pb isotopes. Lithos 182–183, 185–199.

Tang D., Qin K., Sun H., Su B., and Xiao Q. (2012) The role of crustal contamination in the formation of Ni-Cu sulfide deposits in Eastern Tianshan, Xinjiang, Northwest China: Evidence from trace element geochemistry, Re-Os, Sr-Nd, zircon Hf- O, and sulfur isotopes. Journal of Asian Earth Sciences 49, 145–160.

Taranovic V., Ripley E. M., Li C. and Shirey, S.B. (2018) S, O, and Re-Os isotope studies of the Tamarack Igneous Complex: melt-rock interaction during the early stage of Midcontinent Rift Development. Economic Geology 113, 1161–1179.

Thakurta J., Ripley E.M., and Li, C. (2008) Geochemical constraints on the origin of sulfide mineralization in the Duke Island Complex, southeastern Alaska. Geochemistry, Geophysics, Geosystems 9, 1–34.

Tollan P., and Hermann J. (2019). Arc magmas oxidized by water dissociation and hydrogen incorporation in orthopyroxene. Nature Geoscience 12, 667–671.

Tomkins A.G., and Evans K.A. (2015) Separate zones of sulfate and sulfide release from subducted mafic oceanic crust. Earth and Planetary Science Letters 428, 73–83.

Tomkins A.G., Rebryna K.C., Weinberg R.F., and Schaefer B.F. (2012) Magmatic sulfide formation by reduction of oxidized arc basalt. Journal of Petrology 53, 1537–1567.

Villemant B., Jaffrezic H., Joron J.L., and Treuil M. (1981) Distribution coefficients of major and trace-elements-fractional crystallization in the alkali basalt series of Chaine- Des-Puys (Massif Central, France). Geochimica et Cosmochimica Acta 45, 1997–2016.

Wang C.Y., Wei B., Zhou M., Minh Huu D., and Qi, L. (2018) A synthesis of magmatic Ni-Cu- (PGE) sulfide deposits in the ~ 260 Ma Emeishan large igneous province, SW China and northern Vietnam. Journal of Asian Earth Sciences 154, 162–186.

Wang C.Y., Zhou M.F., and Keays, R.R. (2006) Geochemical constraints on the origin of the Permian Baimazhai mafic-ultramafic intrusion, SW China. Contributions to Mineralogy and Petrology152, 309−321.

Wang R.M., Liu D.Q., and Yin D.T. (1987) The conditions of controlling metallogeny of Cu-Ni sulfide ore deposits and the orientation of finding ore Hami, Xinjiang, China. Journal of Mineralogy and Petrology 7, 1–152.

Wang Y.L. (2011) Petrogenesis and mineralization of Heishan intrusion in Beishan area, Gansu. M.Sc. thesis, Chang'an University.

Wei B. (2013) Platinum-group element and Re-Os isotopic compositions of the magmatic Ni-Cu sulfide deposits in the Hongqiling-Chajianling-Piaohechuan region, eastern part of the Central Asian Orogenic Belt. Ph. D. thesis, University of Chinese Academy of Sciences.

Wei B., Wang C.Y., Arndt N.T., Prichard H.M., and Fisher P.C. (2015) Textural relationship of sulfide Ores, PGE, and Sr-Nd-Os isotope compositions of the Triassic Piaohechuan Ni-Cu sulfide deposit in NE China. Economic Geology 110, 2041–2062.

Wei B., Wang C.Y., Lahaye Y., Xie L., and Cao Y. (2019) S and C Isotope Constraints for Mantle-Derived Sulfur Source and Organic Carbon-Induced Sulfide Saturation of Magmatic Ni-Cu Sulfide Deposits in the Central Asian Orogenic Belt, North China. Economic Geology 114, 787–806.

Wei B., Wang C.Y., Li C., and Sun Y. (2013) Origin of PGE-depleted Ni-Cu sulfide mineralization in the Triassic Hongqiling No. 7 orthopyroxenite intrusion, Central Asian Orogenic Belt, northeastern China. Economic Geology 108, 1813–1831.

Windley B.F., Alexeiev D., Xiao W., Kröner A., and Badarch G. (2007) Tectonic models for accretion of the Central Asian Orogenic Belt. Journal of Geological Society 164, 31–47.

Windley B.F., Kröner A., Guo J., Qu G., Li Y., and Zhang C. (2002) Neoproterozoic to Paleozoic geology of the Altai orogen, NW China: new zircon age data and tectonic evolution. Journal of Geology 110, 719–737.

Wood B.J., Bryndzia L.T., and Johnson K.E. (1990) Mantle oxidation state and its relationship to tectonic environment and fluid speciation. Science 248, 337–345.

Woodland A.B., Kornprobst J., and Tabit A. (2006) Ferric iron in orogenic lherzolite massifs and controls of oxygen fugacity in the upper mantle. Lithos 89, 222–241.

Wu F.Y., Zhao G.C., Sun D.Y., Wilde S.A., and Yang J.H. (2007) The Hulan Group: Its role in the evolution of the Central Asian Orogenic Belt of NE China. Journal of Asian Earth Sciences 30, 542–556.

Xia M.-Z., Jiang C.-Y., Li C., and Xia Z.-D. (2013) Characteristics of a newly discovered Ni-Cu sulfide deposit hosted in the Poyi ultramafic intrusion, Tarim Craton, NW China. Economic Geology 108, 1865–1878.

Xiao W.J., Windley B.F., Badarch G., Sun S., Li J.L., Qin K.Z., and Wang Z.H. (2004a) Palaeozoic accretionary and convergent tectonics of the southern Altaids: implications for the lateral growth of Central Asia. Journal of Geological Society, London 161, 339-342.

Xiao W.J., Windley B.F., Huang B.C., Han C.M., Yuan C., Chen H.L., Sun M., Sun S., and Li J.L. (2009) End-Permian to mid-Triassic termination of the accretionary processes of the southern Altaids: implications for the geodynamic evolution, Phanerozoic continental growth, and metallogeny of Central Asia. International Journal of Earth Sciences 98, 1189-1287.

Xiao W.J., Zhang L.C., Qin K.Z., Sun S., and Li J.L. (2004b) Paleozoic accretionary and collisional tectonics of the Eastern Tianshan (China): implications for the continental growth of central Asia. American Journal of Sciences 304, 370-395.

Xie W, Song X.Y., Chen L.M., Deng Y.F., Zheng W.Q., Wang Y.S., Ba D.H., Zhang X.Q., and Luan Y. (2014) Geochemistry insights on the genesis of the subduction-related Heishan magmatic Ni-Cu-(PGE) deposit in Gansu, NW China, at the southern margin of the Central Asian Orogenic Belt. Economic Geology 109, 1563–1583.

Xie W., Song X., Deng Y., Wang Y., and Ba D. (2012) Geochemistry and petrogenetic implications of a Late Devonian mafic- ultramafic intrusion at the southern margin of the Central Asian Orogenic Belt. Lithos 144–145, 209–230.

Xu X., Song S.G., Allen M.B., Ernst R.E., Niu Y.L., and Su L. (2016) An 850–820 Ma LIP dismembered during breakup of the Rodinia supercontinent and destroyed by Early Paleozoic continental subduction in the northern Tibetan Plateau, NW China. Precambrian Research 282, 52–73.

Xu Y., Chung S., Jahn B., and Wu G. (2001) Petrologic and geochemical constraints on the petrogenesis of Permian- Triassic Emeishan flood basalts in southwestern China. Lithos 58, 145-168.

DOI: https://doi.org/10.2138/am-2020-7351. http://www.minsocam.org/

Xue S.C., Qin K.Z., Li C., Tang D.M., Mao Y.J., Qi L., and Ripley E.M. (2016) Geochronological, petrological, and geochemical constraints on Ni-Cu sulfide mineralization in the Poyi ultramafic-troctolitic intrusion in the northeast rim of the Tarim Craton, Western China. Economic Geology 111, 1465–1484.

Yang S.H., and Zhou M.F. (2009) Geochemistry of the∼ 430-Ma Jingbulake mafic-ultramafic intrusion in Western Xinjiang, NW China: implications for subduction related magmatism in the South Tianshan orogenic belt. Lithos 113, 259–273.

Yang S.H., Zhou M.F., Lightfoot P.C., Malpas J., Qu W.J., Zhou J.B., and Kong D.Y (2012) Selective crustal contamination and decoupling of lithophile and chalcophile element isotopes in sulfide-bearing mafic intrusions: an example from the Jingbulake intrusion, Xinjiang, NW China. Chemical Geology 302, 106–118.

Zhang H.L., Cottrell E., Solheid P.A., Kelley K.A., and Hirschmann M.M. (2018) Determination of $Fe^{3+}/\sum Fe$ of XANES basaltic glass standards by Mössbauer spectroscopy and its application to the oxidation state of iron in MORB. Chemical Geology 479, 166–175.

Zhang X., Zhao G., Eizenhöfer P.R., Sun M., Han Y., Hou W., Liu D., Wang B., Liu Q., Xu B., and Yanlin C. (2016) Tectonic transition from Late Carboniferous subduction to Early Permian post-collisional extension in the Eastern Tianshan, NW China: Insights from geochronology and geochemistry of mafic-intermediate intrusions. Lithos 257, 269–281.

Zhang Z., Li K., Li J., Tang W., Chen Y., and Luo Z. (2015) Geochronology and geochemistry of the Eastern Erenhot ophiolitic complex: Implications for the tectonic evolution of the Inner Mongolia-Daxinganling Orogenic Belt. Journal of Asian Earth Sciences 97, 279–293.

Zhang Z.C., Mao J.W., Chai F.M., Yan S.H., Chen B.L., and Pirajno F. (2009) Geochemistry of the Permian Kalatongke mafic intrusions, northern Xinjiang, northwest China: implications for the genesis of magmatic Ni-Cu sulfide deposits. Economic Geology 104, 185–203.

Zhao Y., Xue C., Liu S., Symons D.T.A., Zhao X., Yang Y., and Ke J. (2017) Copper isotope fractionation during sulfide-magma differentiation in the Tulaergen magmatic - Cu deposit, NW China. Lithos 286–287, 206–215.

DOI: https://doi.org/10.2138/am-2020-7351. http://www.minsocam.org/

Zhao Y., Xue C.J., Zhao X.B., Yang Y.Q., Ke J.J., Zu B., and Zhang G.Z. (2016) Origin of anomalously Ni-rich parental magmas and genesis of the Huangshannan Ni-Cu sulfide deposit, Central Asian Orogenic Belt, Northwestern China. Ore Geology Reviews 77, 57–71.

Zhou J.B., and Wilde S.A. (2013) The crustal accretion history and tectonic evolution of the NE China segment of the Central Asian Orogenic Belt. Gondwana Research 23, 1365–1377.

Zhou M., Lesher C.M., Yang Z., Li J., and Sun M. (2004) Geochemistry and petrogenesis of 270 Ma Ni-Cu-(PGE) sulfide-bearing mafic intrusions in the Huangshan district, Eastern Xinjiang, Northwest China: implications for the tectonic evolution of the Central Asian orogenic belt. Chemical Geology 209, 233-257.

Figure captions

Fig. 1. (a) The tectonic context of the central Asian orogenic belt (CAOB) relative to other Cratons (modified after Jahn et al., 2000). (b) A simplified geological map of the CAOB (modified after Xiao et al., 2009) showing the mafic-ultramafic intrusions in the CAOB that formed in arc and post-subduction, extensional settings. (c) A geological map of the western segment of the CAOB. (d) A geological map of the eastern segment of the CAOB.

Fig. 2. Chondrite-normalized rare earth element patterns and primitive mantle-normalized trace element patterns for representative mafic-ultramafic intrusions in the CAOB that were emplaced in arc settings. Data sources: Jinbulake (Yang and Zhou, 2009), Heishan (Xie et al., 2012), Erbutu (Peng et al., 2013). Chondrite and primitive mantle values are from Sun and McDonough (1989).

Fig. 3. Chondrite-normalized rare earth element patterns and primitive mantle-normalized trace element patterns for representative mafic-ultramafic intrusions in the CAOB that were emplaced in post-subduction, extensional settings. Data sources: Huangshanxi (Mao et al., 2014), Hongqiling No.2 (Wei, 2013), and Luodong (Su et al., 2011). Chondrite and primitive mantle values are from Sun and McDonough (1989).

Fig. 4. Plot of Mg# versus Cr# (a) and Mg# versus XFe^{3+} (b) for the spinel of the mafic-ultramafic intrusions in the CAOB, and the Dali picrite from the Emeishan large igneous province. Data sources: Jinbulake, Erbutu, Huangshannan and Tulaergen intrusions (this study), Heishan intrusion (Wang, 2011), Baixintan intrusion (this study; Feng et al., 2017), Luodong intrusion (Su et al., 2011), Hongqiling No.1 and No.2 intrusions (Cao et al., 2019; Wei et al., 2019), Dali picrite (Kamenetsky et al., 2012; Liu et al., 2017).

Fig. 5. Histogram of $\delta^{34}S$ values of sulfides from the Jinbulake, Erbutu, Baixintan and Tulaergen intrusions in the CAOB. The $\delta^{34}S$ values of MORB-type mantle are from Labidi et al. (2014).

DOI: https://doi.org/10.2138/am-2020-7351. http://www.minsocam.org/

Fig. 6. Variation of V/Sc of the primary magma against the degrees of partial melting (F) at given fO_2 (Lee et al., 2005). It is assumed that the mafic-ultramafic intrusions in the CAOB were derived from magmas produced by ~15 to ~20% of partial melting (indicated by the grey shaded area) of the mantle wedge in the spinel stability field.

Fig. 7. Plot of XCr^{3+} of spinel versus $\ln Kd_{Mg/Fe}^{Ol\text{-}Spl}$ for the mafic-ultramafic intrusions in the CAOB, and the Dali picrite in the Emeishan large igneous province. Data sources are the same as those in Fig. 4.

Fig. 8. (a) Comparison of the estimated magma fO_2 of the mafic-ultramafic intrusions in the CAOB and the Dali picrite in the Emeishan large igneous province with the fO_2 of MORBs (FMQ-1 to FMQ+0.5) and arc basalts (FMQ+0.5 to FMQ+6). Data sources: MORBs (Cottrell and Kelley, 2011; Zhang et al., 2018), arc basalts (Woodland et al., 2006). (b) Plot of the magma fO_2 versus the Fo contents of olivine for the mafic-ultramafic intrusions in the CAOB and the Dali picrite in the Emeishan large igneous province. The error bar in (b) represents the uncertainty (FMQ±0.4) of calculated magma fO_2 based on the olivine-spinel oxygen barometer (*c.f.*, Ballhaus et al., 1991). The dashed line outlines the data for the intrusions with tholeiitic, parental magmas.

Fig. 9. (a) Comparison of the magma fO_2 calculated based on olivine-spinel oxygen barometer and the partitioning of V in olivine showing the good agreement of the results obtained by two different methods. The error bars represent the uncertainty of magma fO_2 calculated based on the two methods. (b) Plot of the magma fO_2 calculated based on the olivine-spinel oxygen barometer versus the V/Sc of olivine. There is an overall negative relationship between the magma fO_2 and the V/Sc of olivine. The error bar represents 1 σ standard deviation of the measured V/Sc of olivine.

Fig. 10. Plot of Alz (percentage of tetrahedral sites occupied by Al) versus wt.% TiO_2 of clinopyroxene from the mafic-ultramafic intrusions in the CAOB and the Emeishan large

igneous province. The trends of the arc and rift cumulate are modified after Loucks (1990).

Fig. 11. Comparison of $\delta^{34}S$ values of sulfides and magma fO_2 among the mafic-ultramafic intrusions in the CAOB, the Jinchuan Ni-Cu sulfide deposits in the southern margin of the North China Craton, and the Ni-Cu sulfide deposits in the Emeishan large igneous province. The mafic-ultramafic intrusions in the CAOB overall have fO_2>FMQ+1 and $\delta^{34}S$ similar to the MORB mantle value (-1.6 to +0.6‰; Labidi et al., 2013, 2014), whereas the Ni-Cu sulfide deposits in the intraplate settings have relatively low fO_2 and high $\delta^{34}S$ of sulfides. Data sources: Jinbulake, Erbutu, Baixintan and Tulaergen intrusions (this study), Heishan intrusion (Xie et al., 2014), Hongqiling No.7 intrusion (Wei et al., 2019), Luodong intrusion (Su et al., 2015), Poyi intrusion (Xia et al., 2013), Huangshannan intrusion (Zhao et al., 2016), Huangshandong and Huangshanxi intrusions (Wang et al., 1987), Jinchuan intrusion (Ripley et al., 2005; Duan et al., 2016), the intrusions in the Emeishan large igneous province (Wang et al., 2018).

Fig. 12. Comparison of magma fO_2 values calculated based on the olivine-spinel oxygen barometer with those calculated based on the Fe-Ni exchange between olivine and sulfide melt for the Baixintan (BXT), Huangshannan (HSN), Huangshandong (HSD), Huangshanxi (HSX), Tulaergen (TLEG), and Hongqiling No.1 (HQL) intrusions in the CAOB. The values based on the Fe-Ni exchange between olivine and sulfide liquids are much lower than those based on the olivine-spinel oxygen barometer.

Table 1 S isotopic compositions of the sulfides in the rocks from the Jinbulake, Erbutu, Baixintan and Tulaergen intrusions in the central Asian orogenic belt

Analysis No.	Sample No.	Sulfides	$\delta^{34}S$‰ (V-CDT)	Analysis No.	Sample No.	Sulfides	$\delta^{34}S$‰ (V-CDT)
Jinbulake intrusion				15	18EBT-11	pentlandite	6.2
1	QB-13	pyrrhotite	0.6	16	18EBT-11	pyrrhotite	6.2
2	QB-13	pyrrhotite	0.3	17	18EBT-11	pyrrhotite	6.4
3	QB-13	pyrrhotite	0.0	18	18EBT-5	pentlandite	5.5
4	QB-13	pyrrhotite	0.5	19	18EBT-5	pentlandite	5.5
5	QB-13	pyrrhotite	0.9	20	18EBT-5	pyrrhotite	5.8
6	QB2-102	pyrrhotite	0.9	21	18EBT-5	pyrrhotite	5.3
7	QB2-102	pyrrhotite	0.8	22	18EBT-5	pyrrhotite	5.6
8	QB2-102	pyrrhotite	0.8	23	18EBT-5	chalcopyrite	6.0
9	QB2-102	pyrrhotite	1.3	24	18EBT-5	pentlandite	6.0
10	QB2-78	pyrrhotite	0.1	25	18EBT-5	pentlandite	5.6
11	QB2-78	pyrrhotite	0.2	Baixintan intrusion			
12	QB2-78	pyrrhotite	0.7	1	19BXT-4	chalcopyrite	0.4
13	QB2-78	pyrrhotite	0.5	2	19BXT-4	chalcopyrite	0.3
14	QB-43	pyrrhotite	0.3	3	19BXT-4	pyrrhotite	-0.1
15	QB-43	pentlandite	0.3	4	19BXT-4	pyrrhotite	0.5
16	QB-43	pentlandite	0.3	5	19BXT-4	chalcopyrite	1.1
17	QB-43	pyrrhotite	0.6	6	19BXT-6	pyrite	0.7
18	QB-43	pyrrhotite	0.7	7	19BXT-6	pyrite	0.5
19	QB-43	pentlandite	0.6	8	19BXT-6	pyrite	0.6
20	QB-43	pyrrhotite	0.7	9	19BXT-14	chalcopyrite	0.6
21	QB-65	chalcopyrite	0.9	10	19BXT-14	chalcopyrite	0.1
22	QB-65	chalcopyrite	0.9	11	19BXT-14	pyrrhotite	-0.7
23	QB-65	pyrrhotite	0.6	12	19BXT-14	pyrrhotite	0.1
24	QB-65	pyrrhotite	0.4	13	19BXT-ZK-15	chalcopyrite	1.2
25	QB-65	chalcopyrite	1.3	14	19BXT-ZK-15	pyrrhotite	0.0
26	QB-65	pentlandite	0.7	15	19BXT-ZK-15	chalcopyrite	-0.4
27	QB-65	pyrrhotite	0.9	16	19BXT-ZK-15	chalcopyrite	0.2
28	QB-65	pyrrhotite	0.6	17	19BXT-ZK-15	chalcopyrite	-0.1
Erbutu intrusion				18	19BXT-ZK-15	pentlandite	-0.3
1	18EBT-10	pyrrhotite	7.5	19	19BXT-ZK-15	pentlandite	-0.4
2	18EBT-10	pyrrhotite	7.4	Tulaergen intrusion			
3	18EBT-10	chalcopyrite	7.3	1	TLEG-16	pyrrhotite	0.5
4	18EBT-10	chalcopyrite	5.9	2	TLEG-16	pyrrhotite	0.9
5	18EBT-11	chalcopyrite	6.7	3	TLEG-16	pyrrhotite	0.3
6	18EBT-11	pentlandite	6.2	4	TLEG-16	pentlandite	0.4
7	18EBT-11	pentlandite	6.0	5	TLEG-16	pyrrhotite	0.3
8	18EBT-11	chalcopyrite	6.7	6	TLEG-19	pyrrhotite	0.2
9	18EBT-11	chalcopyrite	6.9	7	TLEG-19	pyrrhotite	-0.2
10	18EBT-11	pentlandite	6.2	8	TLEG-19	pyrrhotite	0.3
11	18EBT-11	pentlandite	6.7	9	TLEG-19	pyrrhotite	0.4
12	18EBT-11	chalcopyrite	6.9	10	TLEG-26	chalcopyrite	0.5
13	18EBT-11	pentlandite	6.4	11	TLEG-26	pyrrhotite	0.2
14	18EBT-11	pentlandite	5.9				

Fig. 1

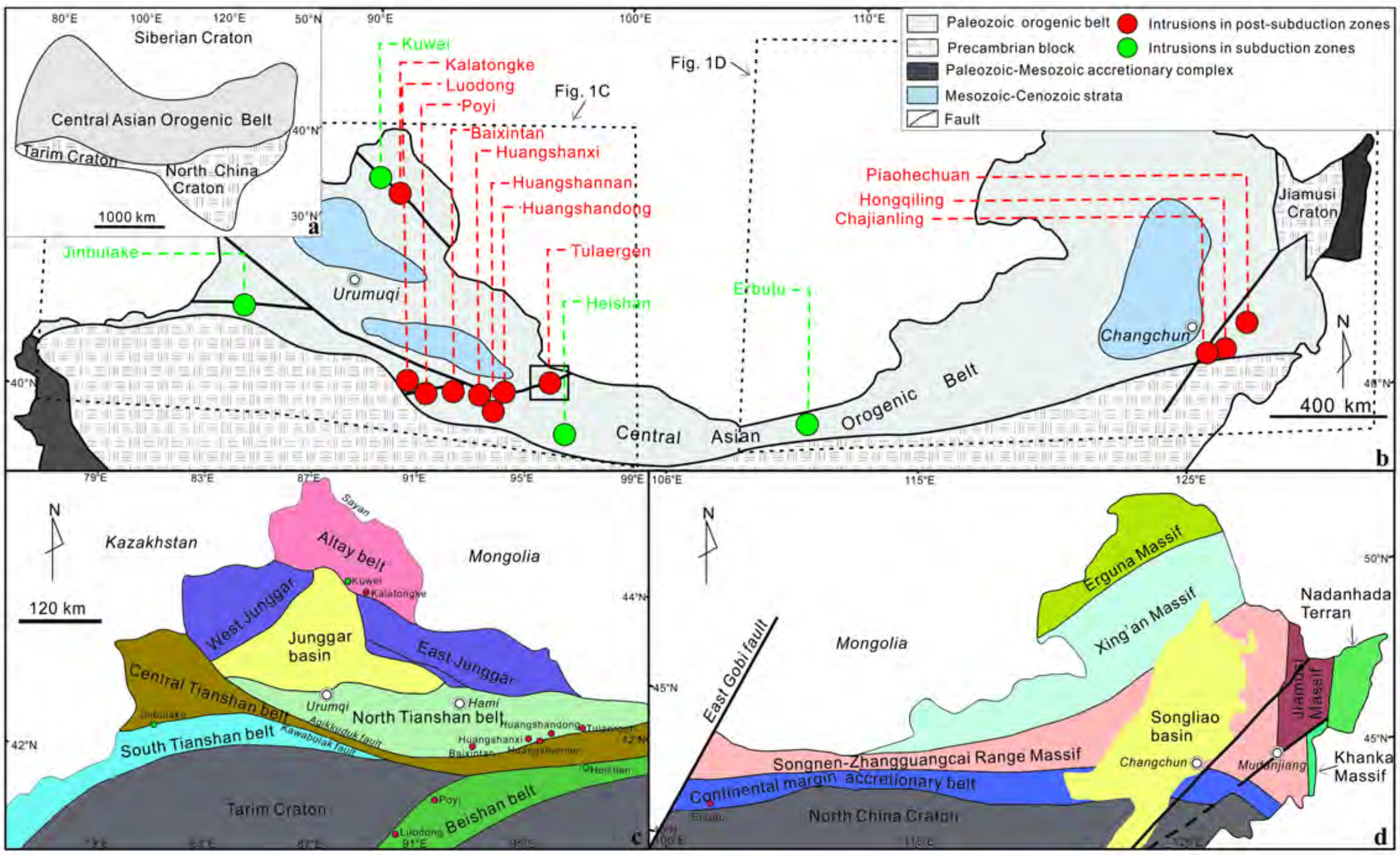
Siberian Craton
Central Asian Orogenic Belt
Tarim Craton
North China Craton
1000 km
Paleozoic orogenic belt
Precambrian block
Paleozoic-Mesozoic accretionary complex
Mesozoic-Cenozoic strata
Fault
Intrusions in post-subduction zones
Intrusions in subduction zones
Kuwei
Kalatongke
Luodong
Poyi
Baixintan
Huangshanxi
Huangshannan
Huangshandong
Tulaergen
Heishan
Jinbulake
Erbulu
Fig. 1C
Fig. 1D
Urumuqi
Piaohechuan
Hongqiling
Chajianling
Jiamusi Craton
Changchun
Central Asian Orogenic Belt
400 km
a
b
Kazakhstan
Mongolia
Altay belt
Sayan
West Junggar
Junggar basin
East Junggar
Central Tianshan belt
North Tianshan belt
South Tianshan belt
Urumqi
Hami
Tarim Craton
Beishan belt
120 km
c
Mongolia
East Gobi fault
Erguna Massif
Xing'an Massif
Songliao basin
Songnen-Zhangguangcai Range Massif
Continental margin accretionary belt
North China Craton
Nadanhada Terran
Jiamusi Massif
Khanka Massif
Changchun
Mudanjiang
d

Fig. 2

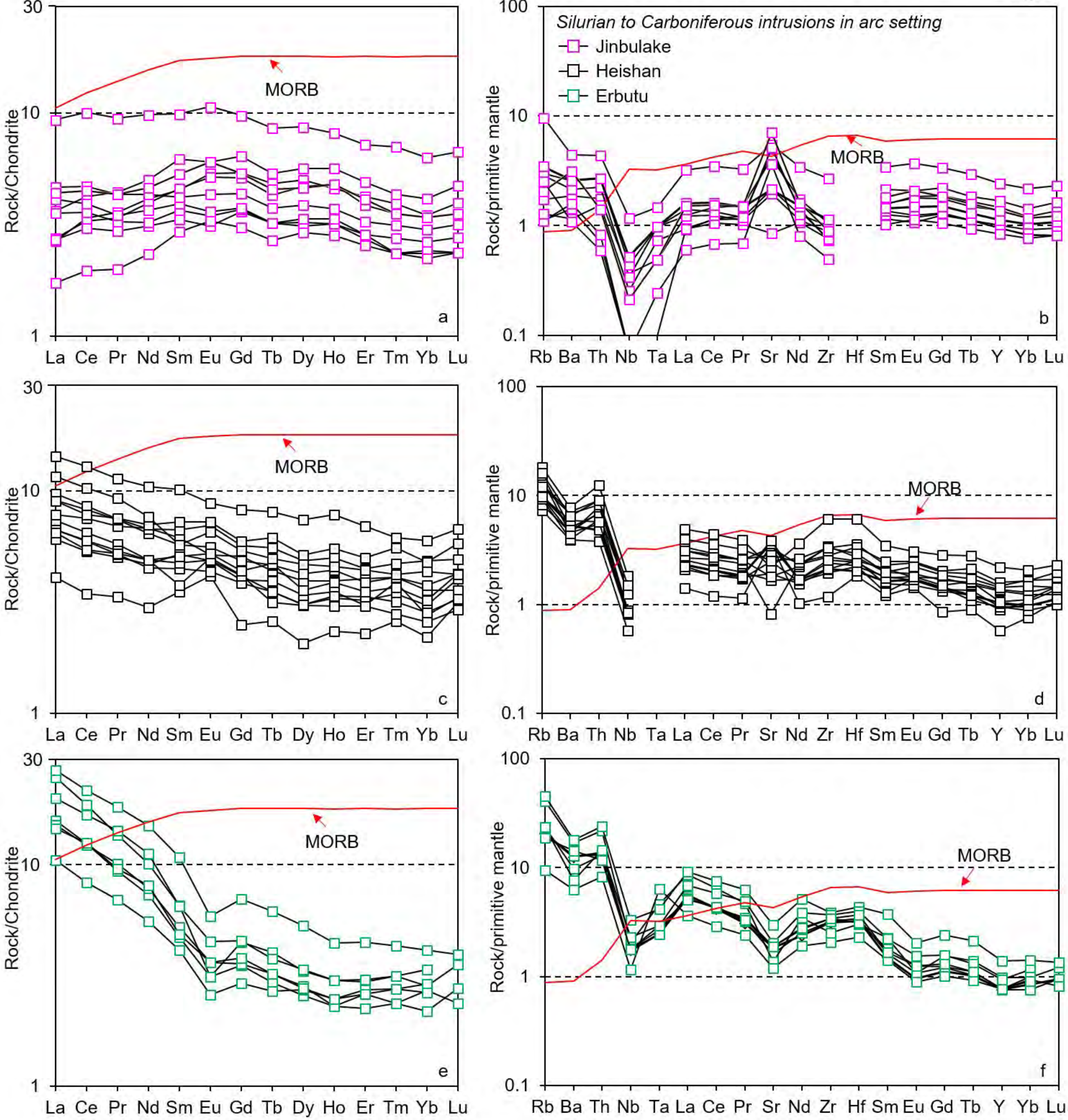
Silurian to Carboniferous intrusions in arc setting
Jinbulake
Heishan
Erbutu
MORB
Rock/Chondrite
Rock/primitive mantle
a
b
c
d
e
f
La Ce Pr Nd Sm Eu Gd Tb Dy Ho Er Tm Yb Lu
Rb Ba Th Nb Ta La Ce Pr Sr Nd Zr Hf Sm Eu Gd Tb Y Yb Lu
30
10
1
100
0.1

Fig. 3

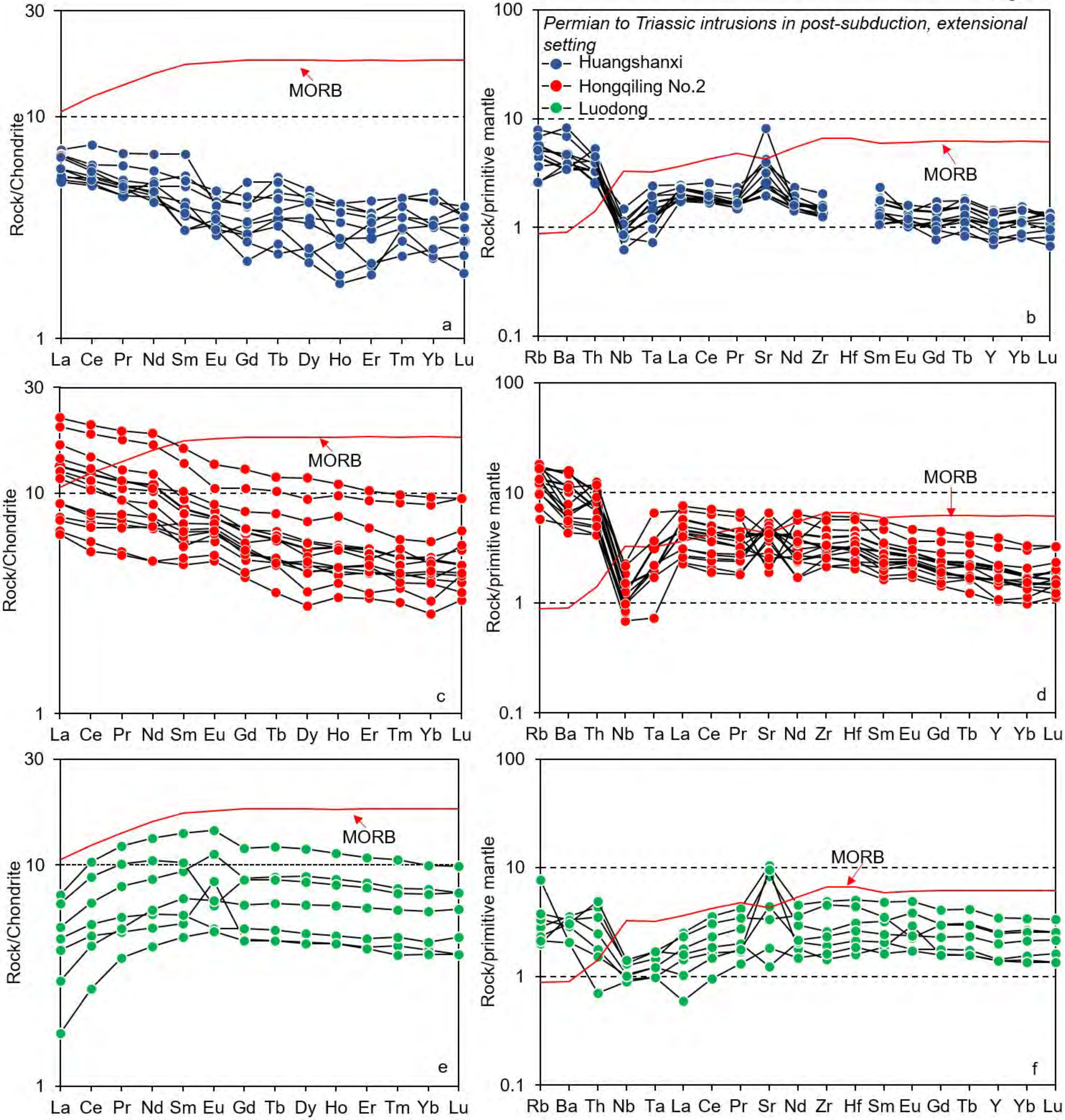
Permian to Triassic intrusions in post-subduction, extensional setting
Huangshanxi
Hongqiling No.2
Luodong
MORB
Rock/Chondrite
Rock/primitive mantle
La Ce Pr Nd Sm Eu Gd Tb Dy Ho Er Tm Yb Lu
Rb Ba Th Nb Ta La Ce Pr Sr Nd Zr Hf Sm Eu Gd Tb Y Yb Lu
a
b
c
d
e
f
30
10
1
100
0.1

Fig. 4

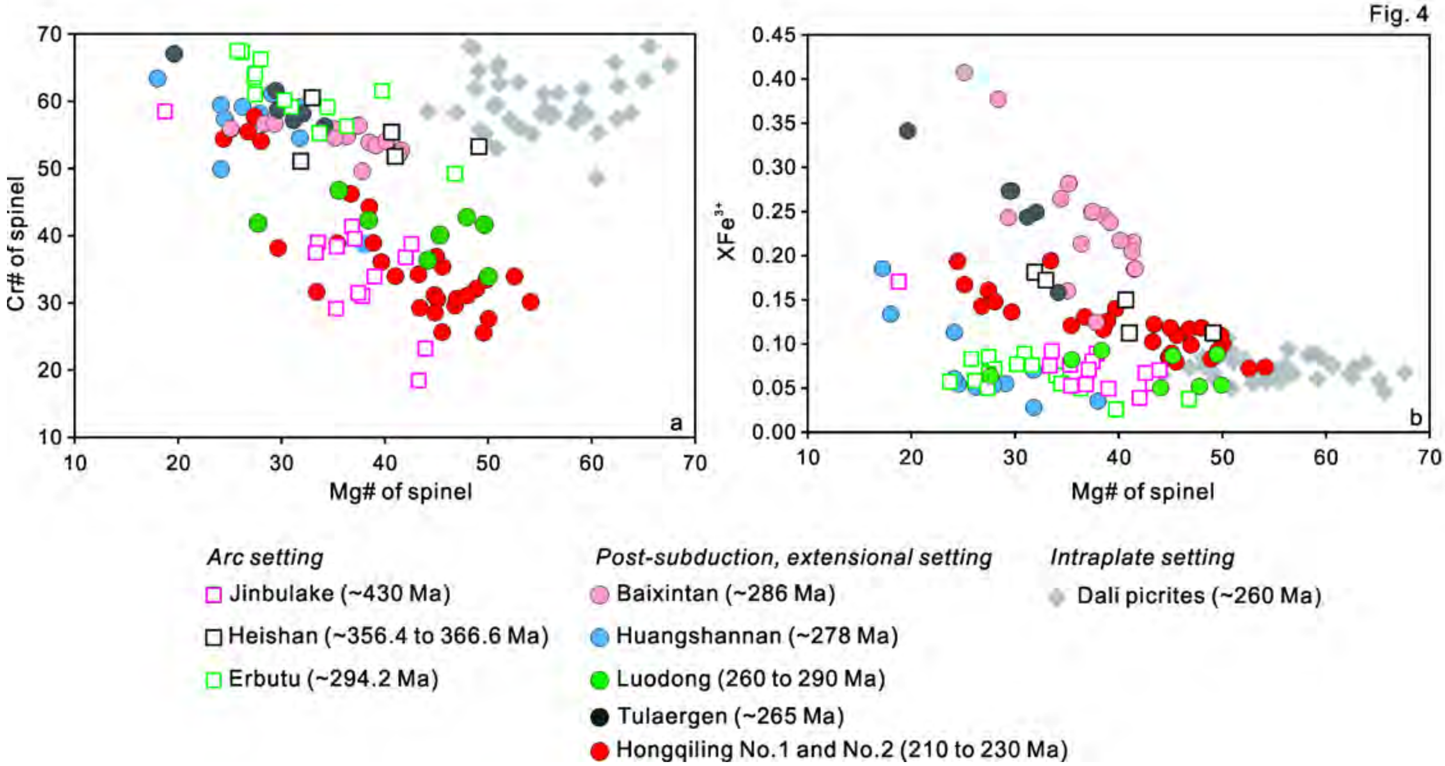
a
Cr# of spinel
Mg# of spinel
b
XFe3+
Mg# of spinel
Arc setting
Jinbulake (~430 Ma)
Heishan (~356.4 to 366.6 Ma)
Erbutu (~294.2 Ma)
Post-subduction, extensional setting
Baixintan (~286 Ma)
Huangshannan (~278 Ma)
Luodong (260 to 290 Ma)
Tulaergen (~265 Ma)
Hongqiling No.1 and No.2 (210 to 230 Ma)
Intraplate setting
Dali picrites (~260 Ma)

DOI: https://doi.org/10.2138/am-2020-7351. http://www.minsocam.org/

Fig. 5

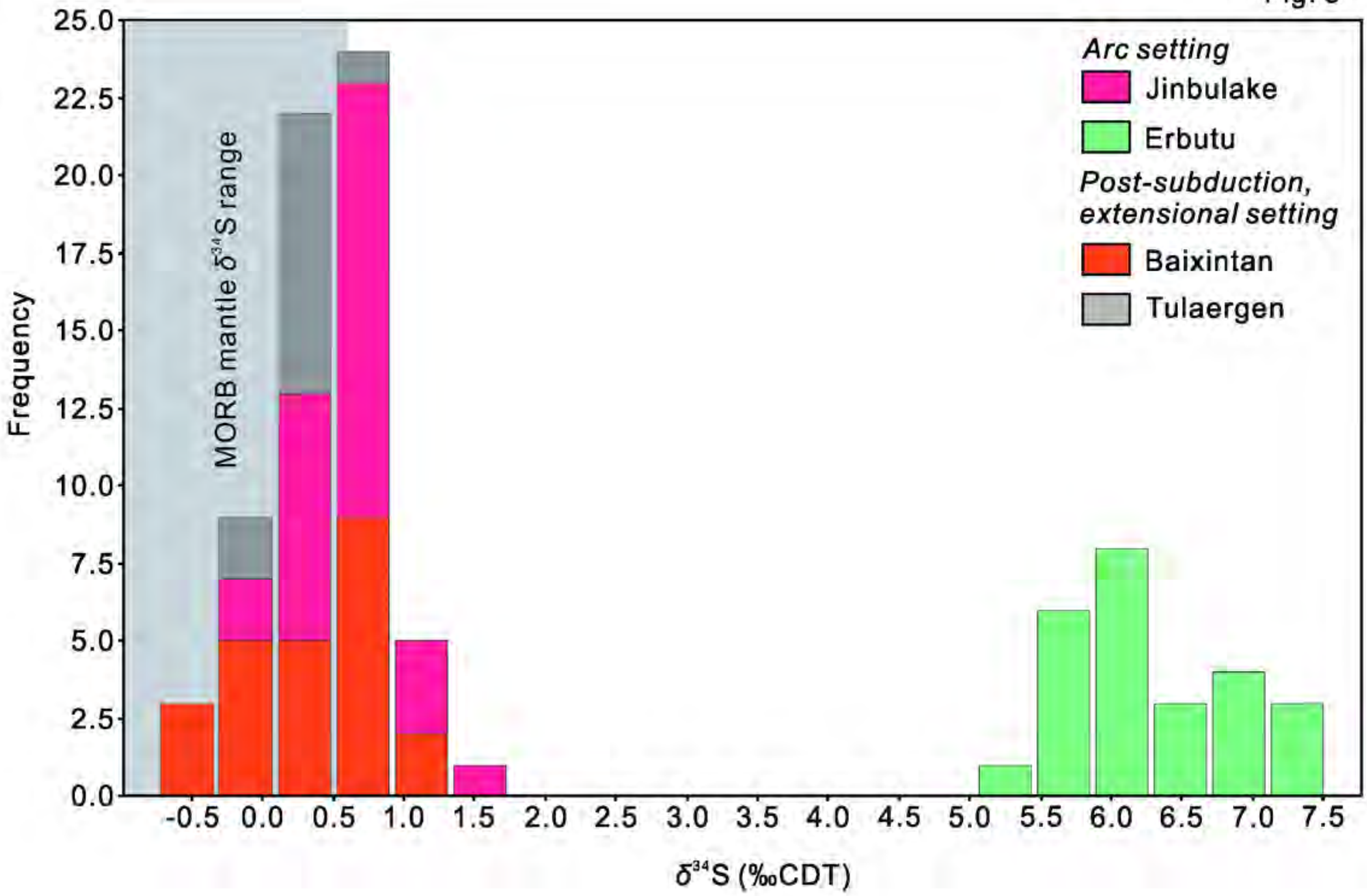

DOI: https://doi.org/10.2138/am-2020-7351. http://www.minsocam.org/

Fig. 6

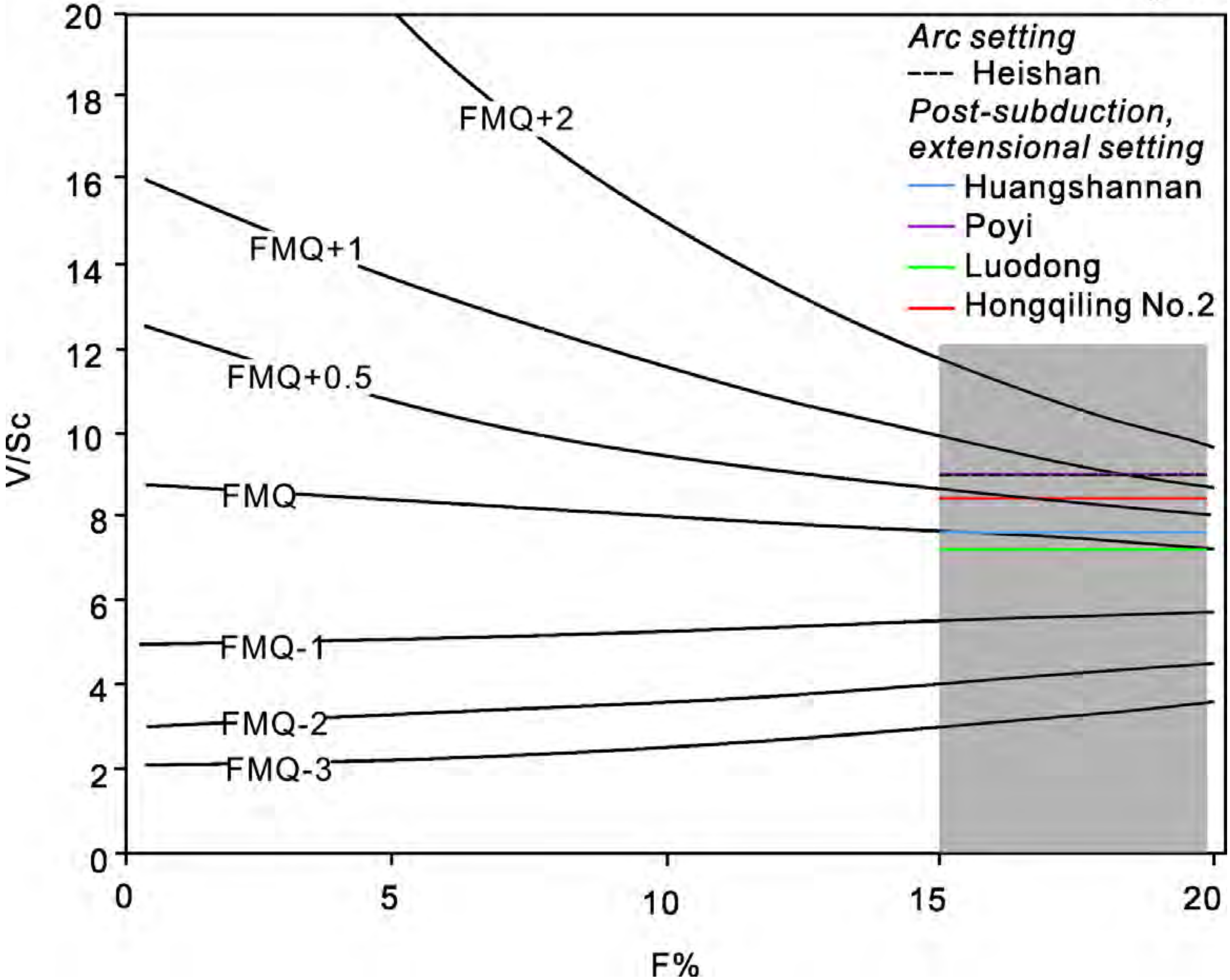

DOI: https://doi.org/10.2138/am-2020-7351. http://www.minsocam.org/

Fig. 7

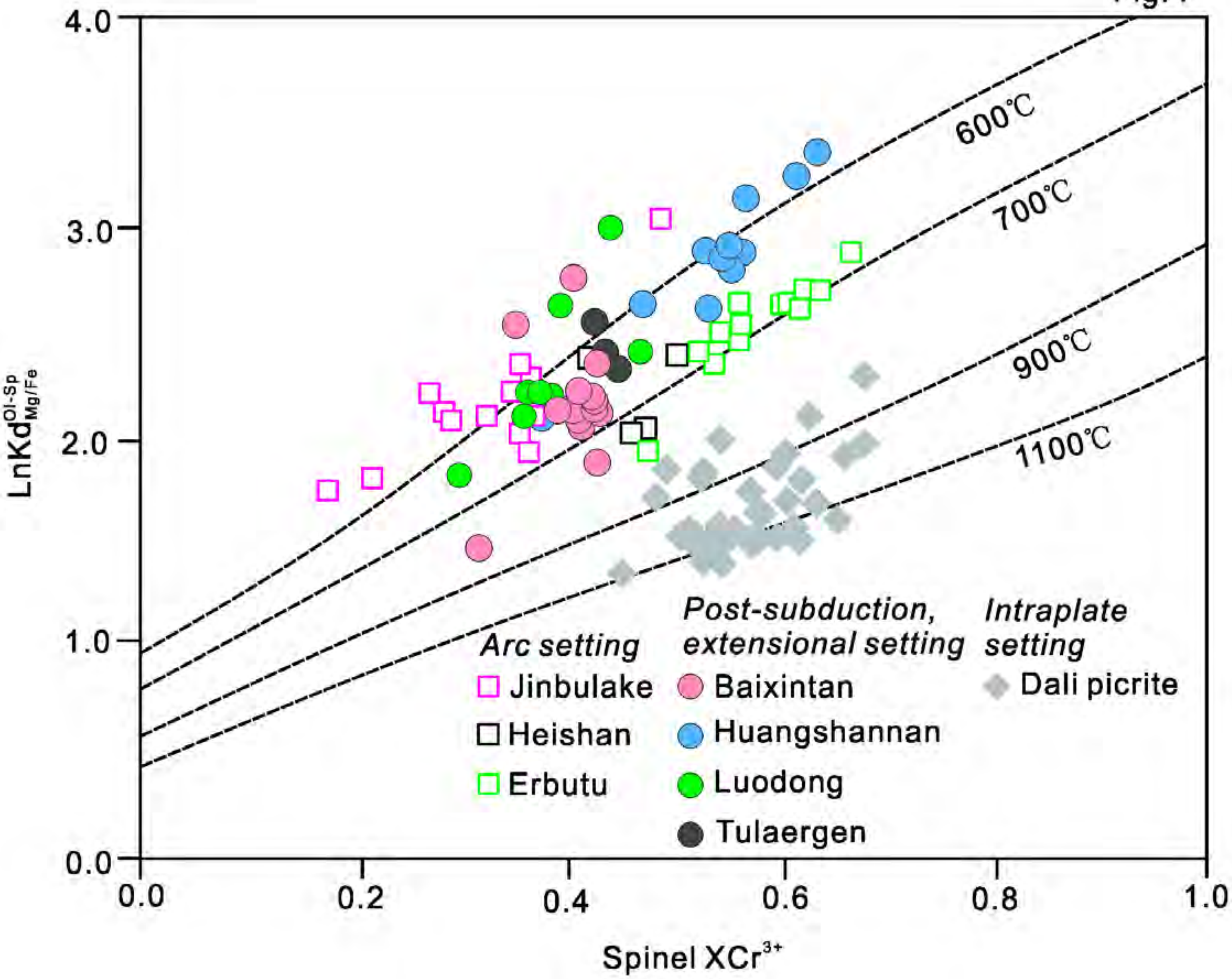

Fig. 8

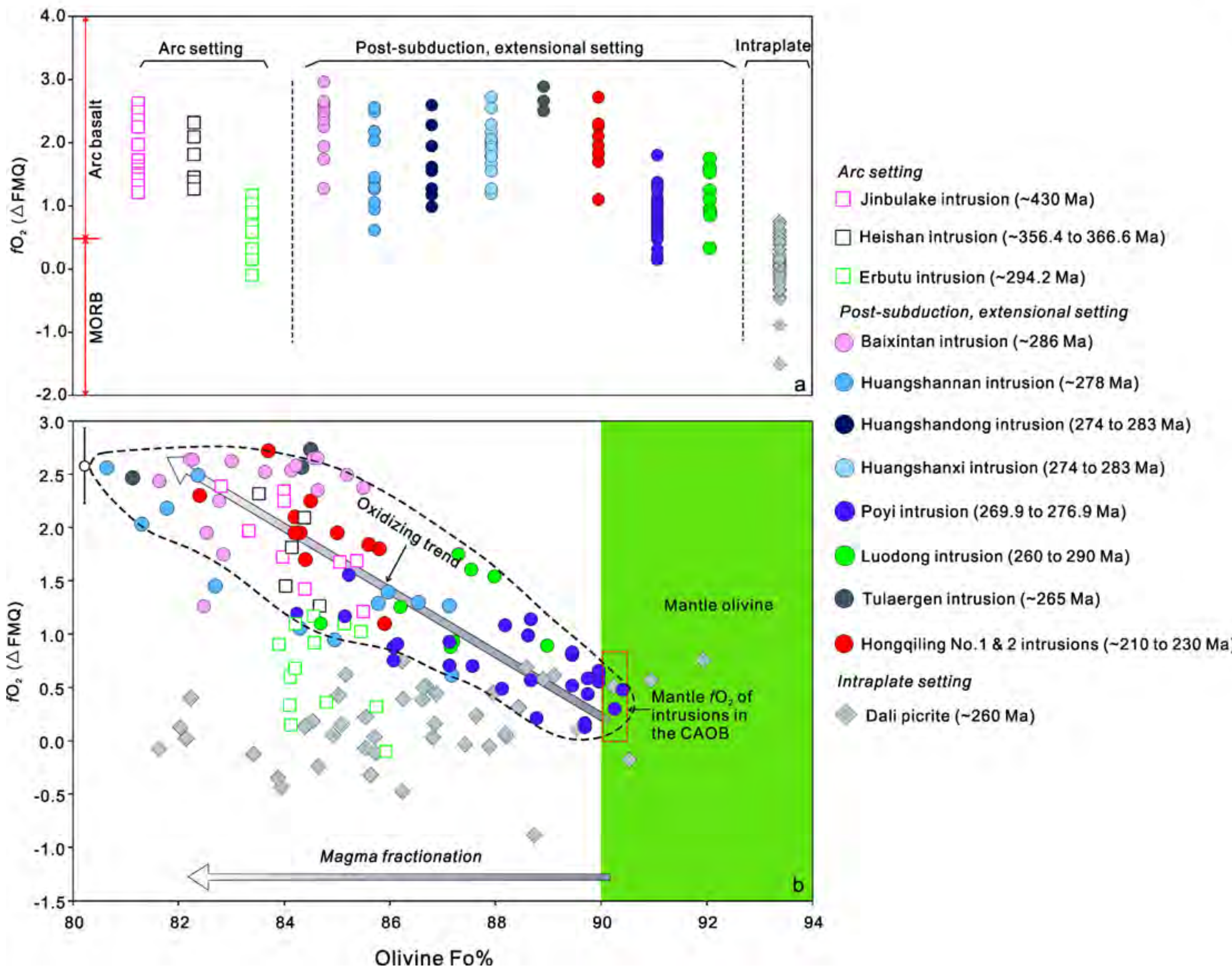
Arc setting
Post-subduction, extensional setting
Intraplate
Arc basalt
MORB
fO2 (ΔFMQ)
a
Oxidizing trend
Mantle olivine
Mantle fO2 of intrusions in the CAOB
Magma fractionation
b
Olivine Fo%
Arc setting
Jinbulake intrusion (~430 Ma)
Heishan intrusion (~356.4 to 366.6 Ma)
Erbutu intrusion (~294.2 Ma)
Post-subduction, extensional setting
Baixintan intrusion (~286 Ma)
Huangshannan intrusion (~278 Ma)
Huangshandong intrusion (274 to 283 Ma)
Huangshanxi intrusion (274 to 283 Ma)
Poyi intrusion (269.9 to 276.9 Ma)
Luodong intrusion (260 to 290 Ma)
Tulaergen intrusion (~265 Ma)
Hongqiling No.1 & 2 intrusions (~210 to 230 Ma)
Intraplate setting
Dali picrite (~260 Ma)

Fig. 9

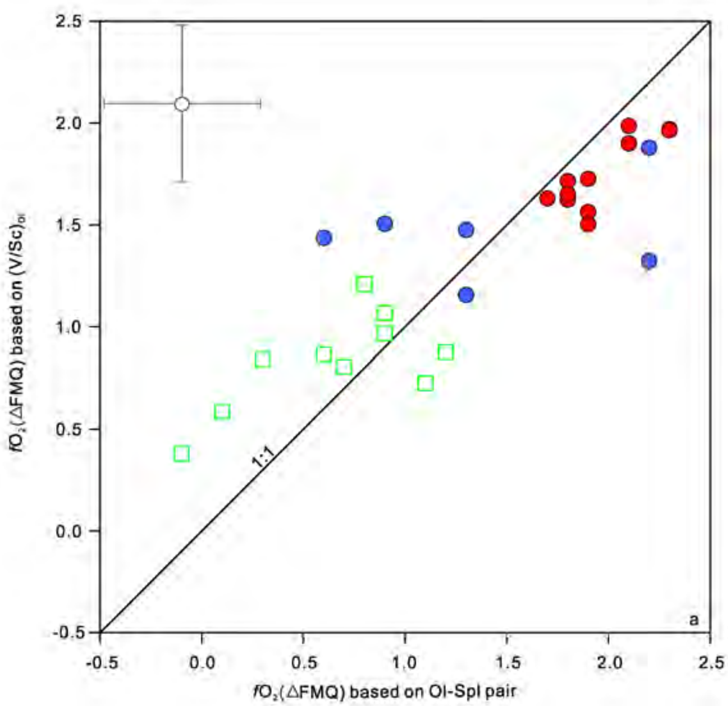
2.5
2.0
1.5
1.0
0.5
0.0
-0.5
1:1
a
-0.5
0.0
0.5
1.0
1.5
2.0
2.5
fO_2(ΔFMQ) based on (V/Sc)$_{ol}$
fO_2(ΔFMQ) based on Ol-Spl pair

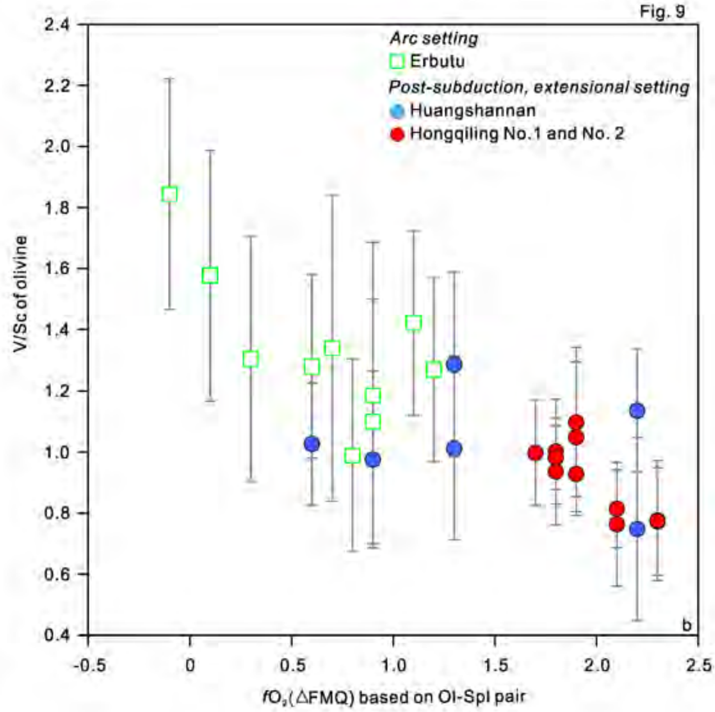
Arc setting
Erbutu
Post-subduction, extensional setting
Huangshannan
Hongqiling No.1 and No. 2
2.4
2.2
2.0
1.8
1.6
1.4
1.2
1.0
0.8
0.6
0.4
V/Sc of olivine
b
-0.5
0
0.5
1.0
1.5
2.0
2.5
fO_2(ΔFMQ) based on Ol-Spl pair

Fig. 10

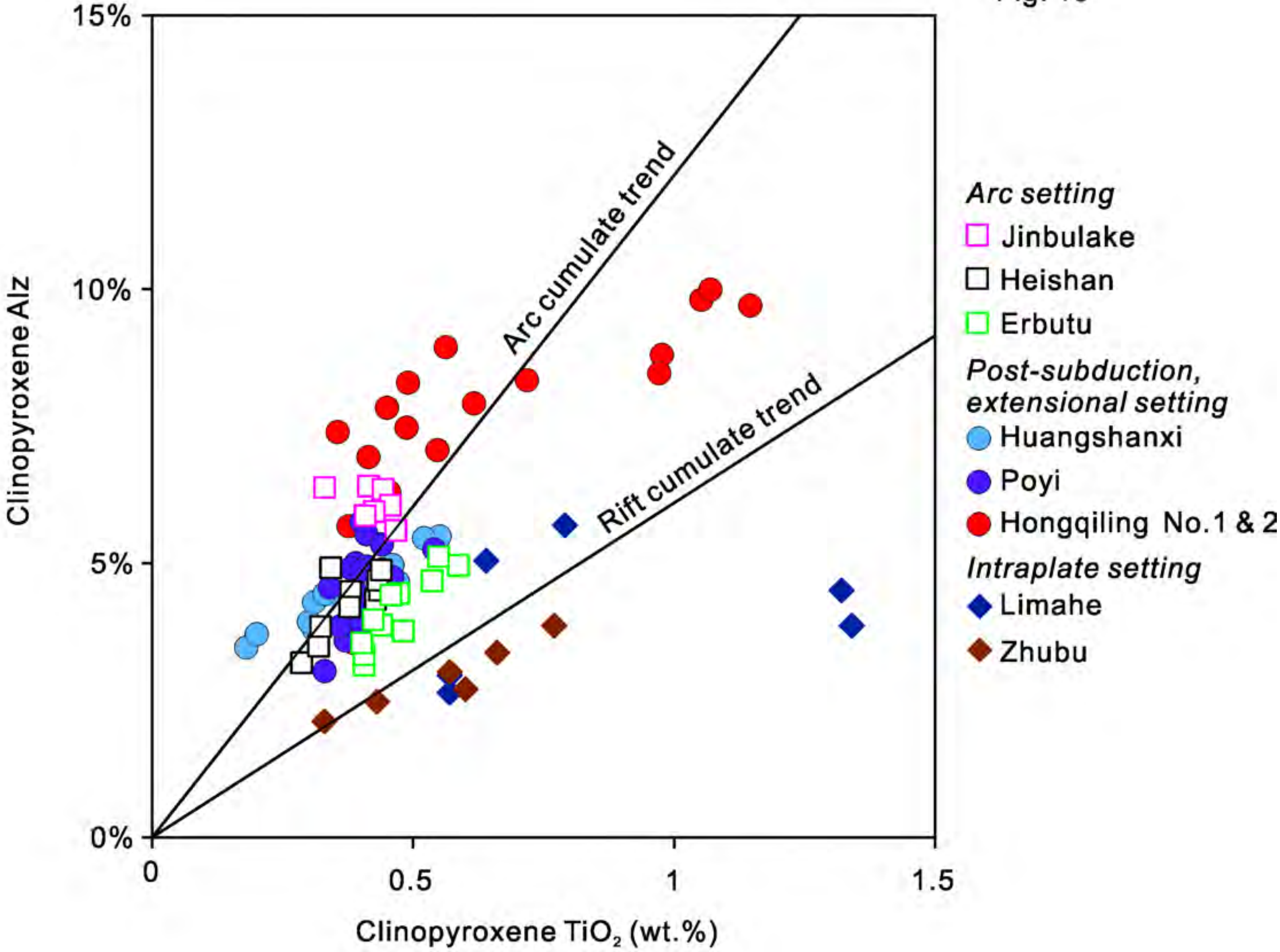
15%
10%
5%
0%
0
0.5
1
1.5
Clinopyroxene Alz
Clinopyroxene TiO₂ (wt.%)
Arc cumulate trend
Rift cumulate trend
Arc setting
Jinbulake
Heishan
Erbutu
Post-subduction, extensional setting
Huangshanxi
Poyi
Hongqiling No.1 & 2
Intraplate setting
Limahe
Zhubu

Fig. 11

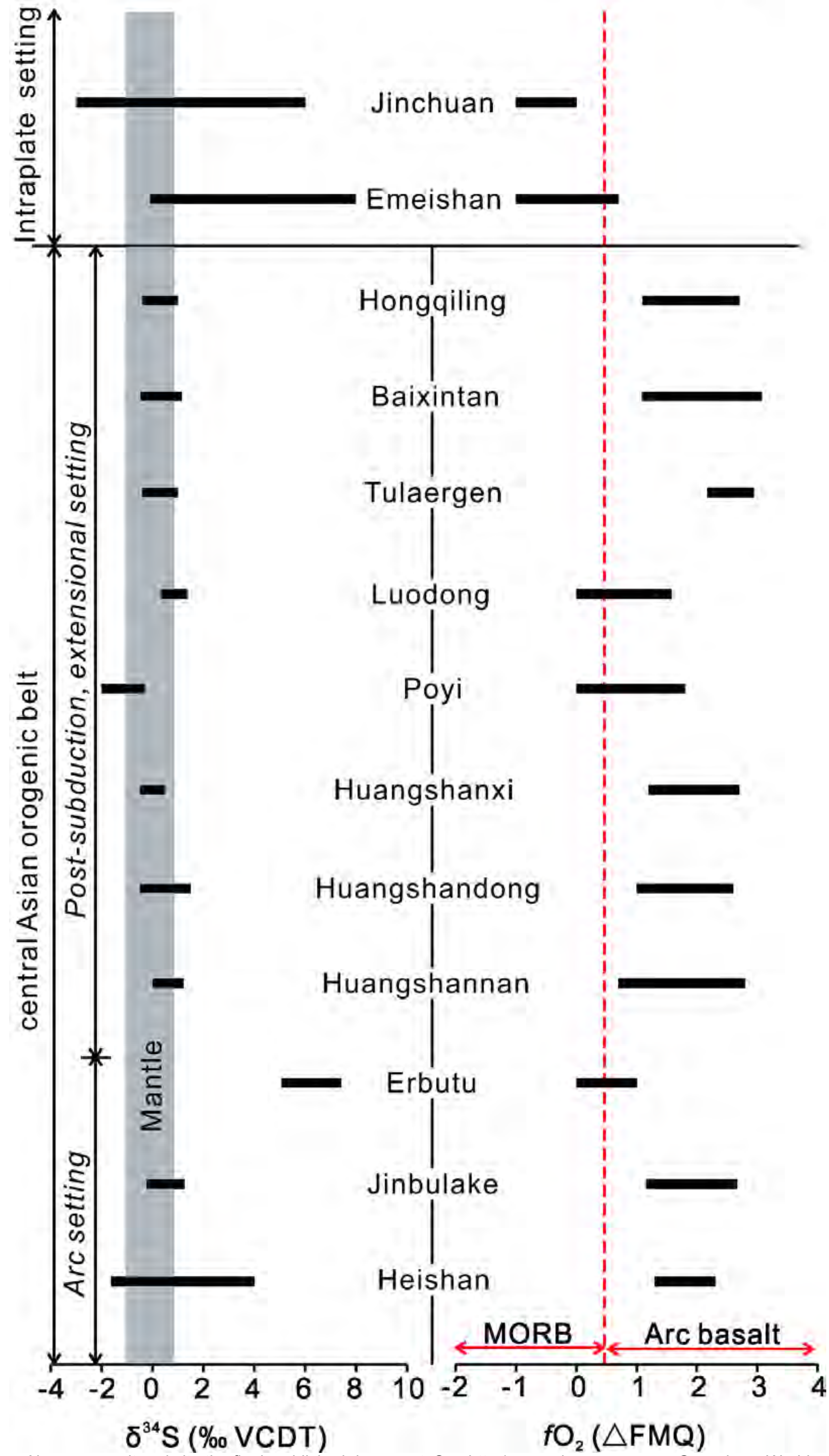
Intraplate setting
central Asian orogenic belt
Post-subduction, extensional setting
Arc setting
Mantle
Jinchuan
Emeishan
Hongqiling
Baixintan
Tulaergen
Luodong
Poyi
Huangshanxi
Huangshandong
Huangshannan
Erbutu
Jinbulake
Heishan
MORB
Arc basalt
-4 -2 0 2 4 6 8 10
-2 -1 0 1 2 3 4
δ^{34}S (‰ VCDT)
fO_2 (△FMQ)

Fig. 12

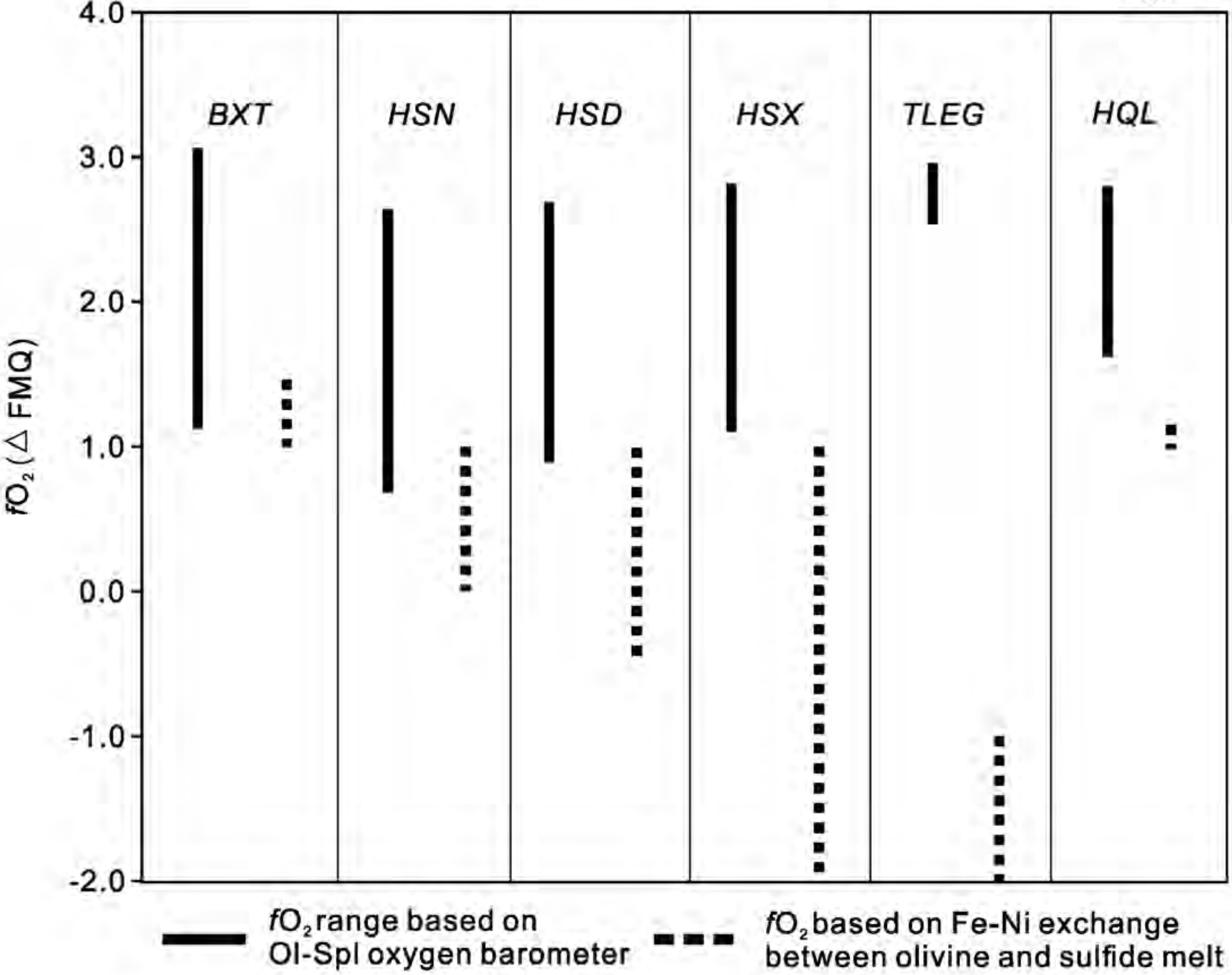
4.0
3.0
2.0
1.0
0.0
-1.0
-2.0
fO2 (△ FMQ)
BXT
HSN
HSD
HSX
TLEG
HQL
fO2 range based on Ol-Spl oxygen barometer
fO2 based on Fe-Ni exchange between olivine and sulfide melt